iScience

Article

Adipocyte-specific Steap4 deficiency reduced thermogenesis and energy expenditure in mice

Graphical abstract

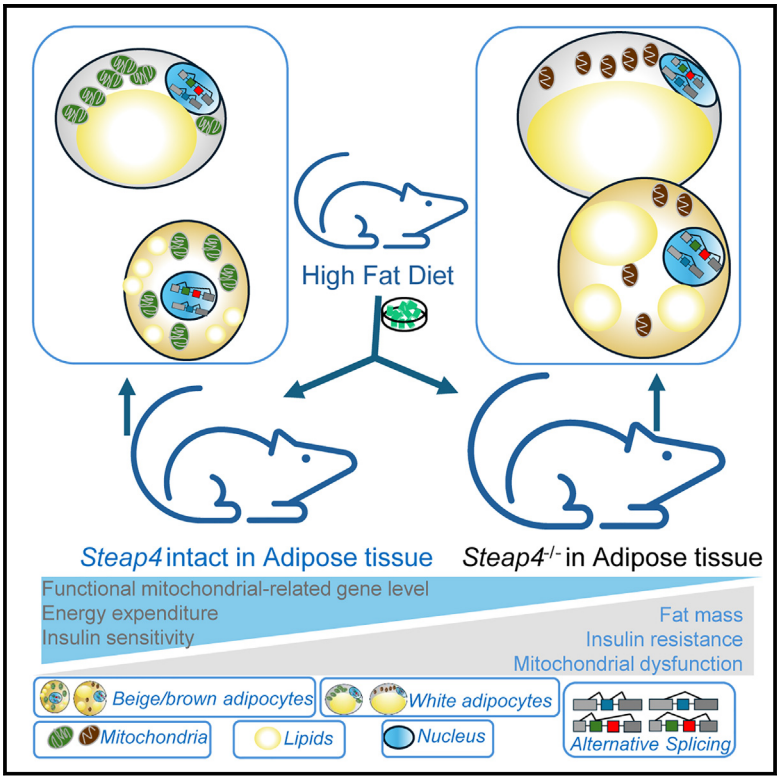

Highlights

- Steap4 regulates thermogenesis, energy expenditure, and adiposity
- Steap4 deficiency leads to mitochondrial dysfunction in adipocytes
- Steap4 interacts with mitochondrial proteins and splicing-associated proteins
- Steap4 regulates alternative splicing of genes involved in mitochondrial functions

Authors

Han Wang, Lizi Zhang, Xing Chen, ..., Xiaoxia Li, Katarzyna Bulek, Xiao Li

Correspondence

xiao.li9@case.edu

In brief

Biological sciences; Endocrinology; Natural sciences; Physiology

Wang et al., 2025, iScience *28*, 111903
February 21, 2025
https://doi.org/10.1016/j.isci.2025.111903

CellPress

iScience

CellPress
OPEN ACCESS

Article

Adipocyte-specific Steap4 deficiency reduced thermogenesis and energy expenditure in mice

Han Wang,[1,2,3] Lizi Zhang,[1,2] Xing Chen,[1,2] Lingzi Hong,[3] Junjie Zhao,[3] Wen Qian,[3] Lam Khue Pham,[1,2] Belinda Willard,[4] Xiaoxia Li,[3] Katarzyna Bulek,[3] and Xiao Li[1,2,5,6,*]

[1]Department of Biochemistry, School of Medicine, Case Western Reserve University, Cleveland, OH 44106, USA
[2]Center for RNA Science and Therapeutics, School of Medicine, Case Western Reserve University, Cleveland, OH 44106, USA
[3]Department of Inflammation and Immunity, Lerner Research Institute, Cleveland Clinic, Cleveland, OH 44106, USA
[4]Proteomics and Metabolomics Core, Lerner Research Institute, Cleveland Clinic, Cleveland, OH 44106, USA
[5]Department of Computer and Data Sciences, School of Engineering, Case Western Reserve University, Cleveland,OH 44106, USA
[6]Lead contact
*Correspondence: xiao.li9@case.edu
https://doi.org/10.1016/j.isci.2025.111903

SUMMARY

Six-transmembrane protein of prostate 4 (Steap4), highly expressed in adipose tissue, is associated with metabolic homeostasis. Dysregulated adipose and mitochondrial metabolism contributes to obesity, highlighting the need to understand their interplay. Whether and how Steap4 influences mitochondrial function, adipocytes, and energy expenditure remain unclear. Adipocyte-specific *Steap4*-deficient mice exhibited increased fat mass and severe insulin resistance in our high-fat diet model. Mass spectrometry identified two classes of Steap4 interactomes: mitochondrial proteins and proteins involved in splicing. RNA sequencing (RNA-seq) analysis of white adipose tissue demonstrated that Steap4 deficiency altered RNA splicing patterns with enriched mitochondrial functions. Indeed, Steap4 deficiency impaired respiratory chain complex activity, causing mitochondrial dysfunction in white adipose tissue. Consistently, brown adipocyte-specific Steap4 deficiency impaired mitochondrial function, increased brown fat whitening, reduced energy expenditure, and exacerbated insulin resistance in a high-fat model. Overall, our study highlights Steap4's critical role in modulating adipocyte mitochondrial function, thereby controlling thermogenesis, energy expenditure, and adiposity.

INTRODUCTION

Obesity has been recognized as a significant risk factor for several health conditions, including type 2 diabetes (T2D), non-alcoholic fatty liver disease (NAFLD), and cardiovascular disease.[1] Emerging evidence suggests that adipose tissue dysfunction is a critical component of obesity-associated pathologies contributing to metabolic disorders.[2,3] Both humans and mice possess two major types of adipose tissue: white adipose tissue (WAT) and brown adipose tissue (BAT).[4,5] Notably, mitochondria, as the primary energy-producing organelles, play a crucial role in maintaining the metabolic homeostasis of WAT and BAT.[6,7] In particular, mitochondria-rich brown and beige adipocytes, also known as thermogenic adipocytes, enable heat generation and energy expenditure through UCP1-mediated uncoupling of oxidative phosphorylation.[8] Notably, BAT activity is inversely correlated with human obesity and diet-induced murine obesity models.[5,9] Individuals with higher BAT activity tend to have a healthier metabolic profile and a lower risk of obesity or related metabolic disorders; in contrast, decreased BAT activity or impaired BAT function is associated with a higher susceptibility to obesity and metabolic complications.[10–13]

It has been reported that six-transmembrane protein of prostate 4 (Steap4), a metalloreductase, also known as tumor-necrosis factor (TNF)-induced adipose-related protein (TIARP) or six-transmembrane protein of the prostate 2 (STAMP2), might play an important role in coordinating glucose/lipid metabolism and inflammation.[14–17] Mouse global deficiency of Steap4 exerts pronounced inflammation in their visceral adipose tissue, and these mice develop spontaneous metabolic disorders on a normal chow diet.[14] While these findings suggest that Steap4 may play a protective role in metabolic-related pathologies, the molecular and cellular mechanisms of action of Steap4, particularly its role in adipocyte, remain largely unclear.

Herein, we report a previously unidentified function of Steap4 in the regulation of adipocyte thermogenesis beyond its metalloreductase capacity. We found that adipocyte-specific Steap4-deficiency led to increased fat mass, reduced energy expenditure, elevated severe insulin resistance and suppressed mitochondrial function in a high-fat diet model. By mass spectrometry analysis, we identified two classes of Steap4 interactomes: mitochondrial proteins and proteins involved in spliceosome. In parallel, transcriptomic analysis revealed the critical role of Steap4 in the mitochondrial respiratory chain and alternative splicing events with enriched functions in mitochondria.

Consistent with Steap4 interactome and transcriptome analysis, Steap4 deficiency indeed led to adipocyte mitochondrial dysfunction with substantial impairment of mitochondrial respiratory chain complex activity. Additionally, thermogenic adipocyte-specific Steap4-deficient mice showed impaired mitochondrial function, increased whitening of brown adipose tissue, reduced energy expenditure, and exacerbated insulin resistance upon high-fat diet (HFD) feeding. Overall, our findings elucidate an unexpected role of Steap4 in regulating adipocyte thermogenesis and energy expenditure by controlling mitochondria function through direct interactions with mitochondrial proteins and modulating alternative splicing via spliceosome interaction.

RESULTS

Steap4 is predominantly expressed in mature adipocytes

GTEx data suggest that STEAP4 exhibits elevated expression level in subcutaneous and visceral adipose tissue compared to other human tissues (Figures 1A and S1A).[18] This expression pattern remains consistent in C57/BL6J wild-type (WT) mice fed with a normal chow diet, underscoring the potential role of Steap4 in adipose tissue (Figure 1B). To investigate the primary source of Steap4 in adipose tissues, we isolated stromal vascular fractions (SVFs, comprising preadipocytes) and mature adipocytes from inguinal white adipose tissue (iWAT), epididymal white adipose tissue (eWAT), and interscapular brown adipose tissue (iBAT). Subsequent analysis of Steap4 expression levels in these depots showed that while preadipocytes exhibited minimal Steap4 expression, mature adipocytes displayed much higher levels of Steap4 expression (Figure 1C), consistent with what observed in 3T3-L1 cells.[14] These findings suggest that mature adipocytes, the primary cellular constituents of adipose tissue responsible for energy storage and endocrine regulation, may serve as a prominent source of Steap4 expression in adipose tissue.

Steap4 deficiency in adipocytes promotes high-fat diet-induced obesity and metabolic dysfunction

Given the high expression pattern of Steap4 in mature adipocytes, we hypothesize that Steap4 may have an impact on diet-induced obesity. To test this hypothesis, we generated adipocyte-specific *Steap4*-deficient (*Steap4*^{AKO}) mice by breeding *Steap4* flox/flox (*Steap4*$^{f/f}$) mice to *Adiponectin*-Cre transgenic mice (Figure S1B). After 12 weeks of HFD feeding, *Steap4*^{AKO} mice gained more weight and had increased fat mass in iWAT, eWAT, and iBAT, compared to sex- and age-matched wild-type controls (*Steap4*$^{f/f}$) (Figures 1D–1F). The *Steap4*^{AKO} mice also exhibited deteriorated glucose tolerance and insulin sensitivity, compared with the *Steap4*$^{f/f}$ mice (Figures 1G and 1H). Further, *Steap4*^{AKO} iWAT displayed increased adipocyte size and more crown-like structure formation compared to the control mice (Figure 1I). We next examined the impact of adipocyte-specific Steap4 depletion on iBAT function. Interestingly, HFD-fed *Steap4*^{AKO} mice displayed accelerated whitening of iBAT and attenuated Ucp1 expression compared with *Steap4*$^{f/f}$ control mice (Figure 1J). Consistently, decreased thermogenic gene expression, including *Ucp1*, *Prdm16*, *Cidea*, *Dio2*, *and Cox8b*, was observed in *Steap4*^{AKO} mice compared to control mice (Figure 1K). Overall, these phenotypes indicated that adipocyte-derived Steap4 may play an important role in adipocyte homeostasis in HFD-induced metabolic disorders.

Mass spectrometry analysis unveils the Steap4 interactome in mitochondria and its contribution to mitochondrial function

To further understand the function of Steap4 in adipocytes, we conducted mass spectrometry-based proteomic analysis to elucidate the Steap4 interactome in mature adipocytes. Remarkably, a total of 91 proteins displayed specific interaction with Steap4 in mature adipocytes, whereas no such interactions were observed in *Steap4* KO cells or WT preadipocytes (SVFs), which exhibit minimal Steap4 expression.

These Steap4 interacting proteins exhibited subcellular localization patterns that closely resemble the localization of Steap4. According to the COMPARTMENTS database,[19] which integrates various sources of evidence on protein localization, Steap4 was primarily found (confidence score >4) in the plasma membrane, endosome, and nucleus, and has minimal evidence (confidence score <1) supporting its localization in peroxisome, Accordingly, 14, 1, and 46 Steap4-interacting proteins showed high-confident (confidence score $\geq$4) localization in the plasma membrane, endosome, and nucleus, whereas no protein showed high-confident localization in peroxisome (Figure 2A; Table S1). Notably, these localization patterns of Steap4 interactome remained similar in human cells (Figure S2A).

Interestingly, 18 Steap4 interacting proteins showed high-confident mitochondrial localization while COMPARTMENTS database presented moderate evidence supporting the localization of Steap4 in mitochondria (confidence score = 1.504). Similar results were observed using MitoCarta3.0[20] and the MitoCoP inventories[21] (Table S2). We suspected it was due to the lower baseline expression of Steap4 in tissue or cell types other than adipose tissue. Steap4 is indeed localized in mitochondria, as reviewed by confocal imaging data (Figure 2B) as well as previously evidenced by the induced expression level in mitochondria in a Dextran Sodium Sulfate (DSS)-induced colitis model.[22]

Consistently, GO enrichment analysis suggested that Steap4 interactome are enriched for proteins related to mitochondria function (Figure 2C; Table S3). Importantly, these Steap4-interacting mitochondria proteins are critical mediators in mitochondria respiration, dysregulation of these proteins would lead to mitochondrial dysfunction and metabolic disorders. For example, we further performed co-immunoprecipitation of Steap4 interacting proteins extracted in mitochondria fraction of iWAT and confirmed mitochondrial aconitase (Aco2) and cytochrome P450 family 1 subfamily B member 1 (Cyp1b1) as interacting proteins of Steap4 (Figure 2D). Based on these results, we hypothesized that Steap4 interacts with mitochondrial proteins and has a critical regulatory function on mitochondria in adipose tissue. Indeed, reduced mitochondrial basal and maximal respiration were observed in iWAT explants from HFD-fed *Steap4*^{AKO} mice compared to those from *Steap4*$^{f/f}$ mice, as assessed by Seahorse (Figure 2E), demonstrating a positive regulatory role of Steap4 exerted in mitochondrial function.

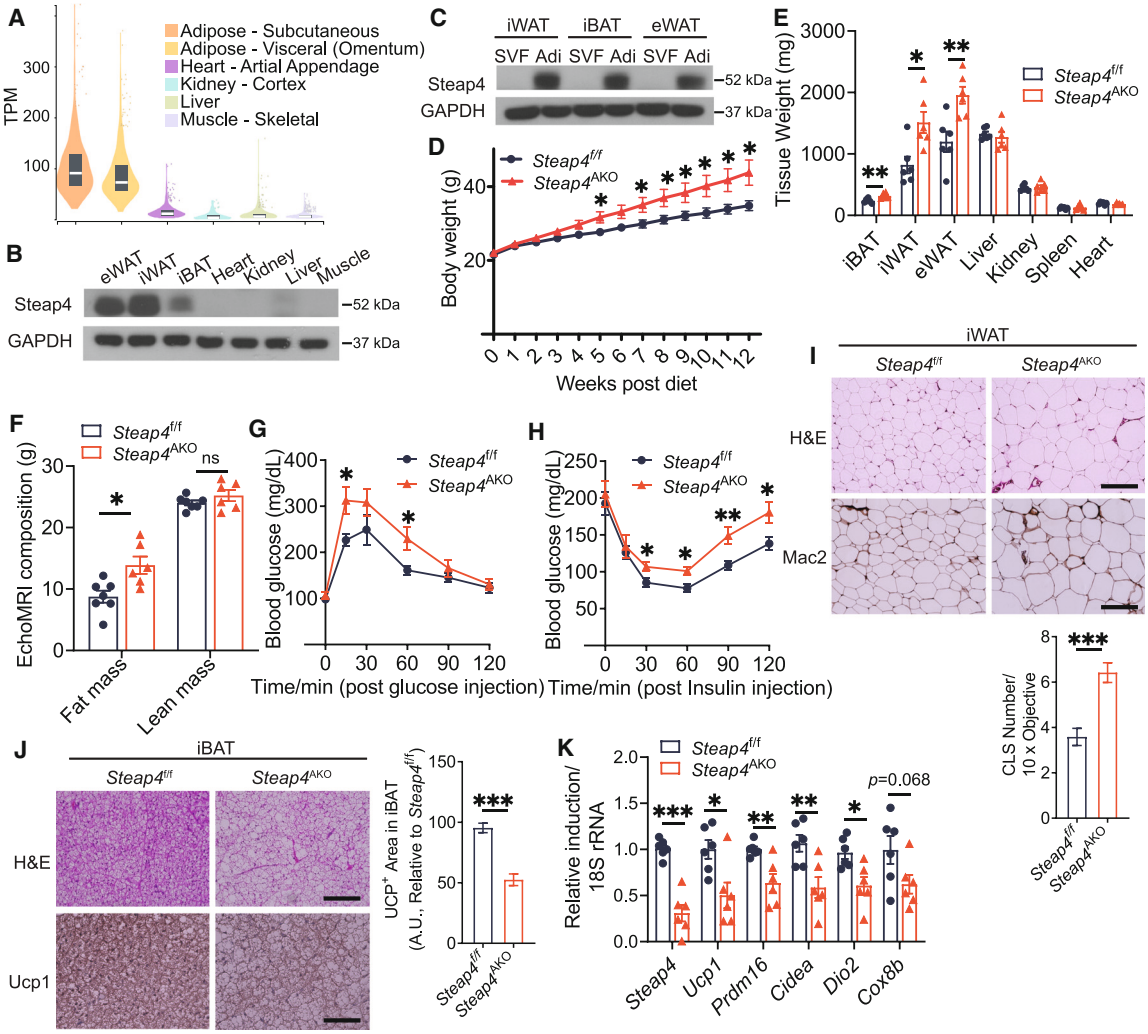

Figure 1. STEAP4 is highly expressed in adipose tissue and mature adipocytes, and its deficiency in adipocytes promotes HFD-induced obesity

(A) Bulk tissue gene expression for STEAP4 in human tissues reported by GTEx.

(B) Steap4 expression measured in selected mouse tissues by western blot.

(C) Steap4 expressions analyzed in isolated SVF (stromal vascular fraction) or mature adipocytes by western blot.

(D) Body weight of *Steap4*$^{f/f}$ and *Steap4*^{AKO} mice fed an HFD diet for 12 weeks (n = 7, 6).

(E) Indicated organs weight from HFD-fed *Steap4*$^{f/f}$ and *Steap4*^{AKO} mice after 12 weeks HFD feeding (n = 6 pairs).

(F) EchoMRI analysis of fat mass and lean mass from *Steap4*$^{f/f}$ and *Steap4*^{AKO} mice after HFD feeding (n = 7, 6).

(G–H) Glucose tolerance test (GTT) and insulin tolerance test (ITT) in HFD-fed *Steap4*$^{f/f}$ and *Steap4*^{AKO} mice (n = 7, 6).

(I) Upper: Representative images (20x) of Hematoxylin and Eosin (H&E) staining and Mac2 staining of iWAT sections from HFD-fed *Steap4*$^{f/f}$ and *Steap4*^{AKO} mice. Scale bars: 150 μm. Lower: Quantification of crown-like structure (CLS) numbers in 10x objective (n = 12 fields).

(J) Left: Representative images of H&E staining and Ucp1 staining of iBAT sections from HFD-fed *Steap4*$^{f/f}$ and *Steap4*^{AKO} mice. Right: Quantification of relative Ucp1^{+} area by ImageJ Software (n = 12 fields). Scale bars: 150 μm (H&E) and 75 μm (Ucp1).

(K) Expression of the indicated mRNAs in iBAT from HFD-fed *Steap4*$^{f/f}$ and *Steap4*^{AKO} mice (n = 6 each group).

Statistical significance for all relevant graphs was determined by two-tailed Student's test. Significance: * $0.01 \leq p < 0.05$, ** $0.001 \leq p < 0.01$, *** $p < 0.001$; ns, not significant. All data represent means ± SEM.

Steap4 deficiency promotes mitochondrial dysfunction via suppression of mitochondrial-related gene expression and electron transport chain complex activity

To further characterize the impact of Steap4 on HFD-induced mitochondrial dysfunction in adipose tissue, we performed RNA-seq on iWAT collected from HFD-fed *Steap4*$^{f/f}$ and *Steap4*^{AKO} mice. A total number of 1,211 genes were identified as differentially expressed genes. Functional GO enrichment analysis revealed that *Steap4*^{AKO} iWAT exhibited increased inflammatory response terms, which is consistent with the elevated inflammatory gene expressions and elevated Mac2^{+} immune cell

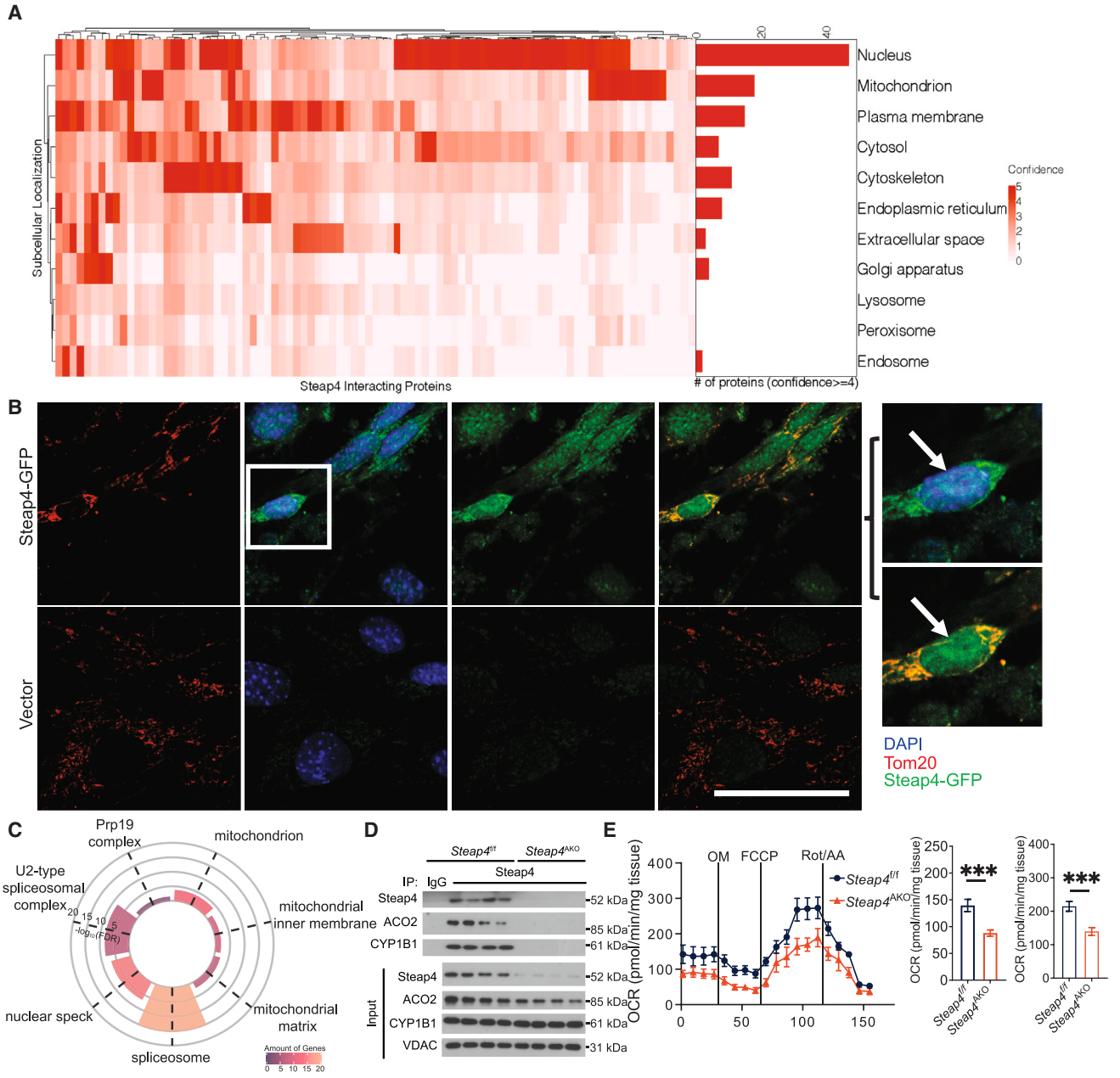

Figure 2. Subcellular localization, functional characterization of Steap4 interactome

(A) Heatmap and bar figure summarizing subcellular localization distribution of Steap4 interactome as defined by COMPARTMENTS database. In the heatmap, each row represents subcellular localization, each column represents a protein that interacts with Steap4 as identified by mass spectrometry analysis, and the color represents the confident score of the subcellular localization of the indicated protein. The bar figure shows the number of Steap4-interacted proteins with high subcellular localization confidence (confidence score ≥ 4).

(B) SVF cells (infected with lentivirus encoding Steap4-GFP) were fixed 4 days after infection and stained for Tom20, followed by imaging analysis. Scale bar: 50 μm. The white arrow indicates Steap4 localization in the nucleus, while mitochondrial localization is shown by the overlap with Tom20 staining.

(C) Circular visualization graph shows the selected significant GO terms (FDR <0.1) for Steap4 interacting proteins. The size of the colored bars in the inner circle represents the significance of each functional term ($-\log_{10}$(FDR)). The color scale represents the number of identified Steap4 interacting proteins in the indicated functional term. Pink outline: mitochondrial proteins; Blue outline: proteins involved in spliceosomes.

(D) CoIP verification of Steap4 interacting proteins extracted in mitochondria fraction of iWAT from HFD-fed *Steap4*$^{f/f}$ and *Steap4*^{AKO} mice. Each lane indicates an individual sample.

(E) Left: Real-time kinetic rate of oxygen consumption (OCR) of iWAT explants from HFD-fed *Steap4*$^{f/f}$ and *Steap4*^{AKO} mice ($n = 5$ each group). Right: Calculated basal and maximum respiration. OCR levels were normalized to iWAT explant weights.

Statistical significance for all relevant graphs was determined by two-tailed Student's t test. Significance: ***$p < 0.001$. All data represent means ± SEM.

infiltration in *Steap4*^{AKO} iWAT that were observed in Figure 1I (Figure 3A; Table S4).

Interestingly, mitochondria-related terms were highly enriched, with genes involved in oxidative phosphorylation (OxPhos), fatty acid oxidation, and mitochondrial respiration electron transfer chain significantly downregulated in *Steap4*^{AKO} iWAT compared with that of *Steap4*$^{f/f}$ (Figures 3A and 3B). Notably, mitochondrial respiratory complexes (or electron transport chain, ETC), including complexes I–V, have a central role in enhancing cellular respiration by creating and sustaining a proton-motive force across the inner mitochondrial membrane. This proton-motive force is then utilized by the ATP synthase complex (complex V) to drive the synthesis of ATP.[23] In the RNA-seq dataset, genes encoding each respiratory chain complex I–V and ATP synthetases were greatly repressed in *Steap4*^{AKO} in the mitochondrial ETC pathway of the iWAT (Figure 3B). Real-time-qPCR (Quantitative real-time PCR) experiments also validated the ameliorated expression of ETC complex components in *Steap4*^{AKO} iWAT compared to *Steap4*$^{f/f}$ iWAT (Figure 3C). Moreover, the mitochondrial respiratory complexes have been observed to organize themselves into higher-order structures called supercomplexes, which further optimize mitochondrial electron transfer and ATP production.[24,25] Significantly, we found that mitochondria from iWAT of HFD-fed *Steap4*^{AKO} mice had impaired supercomplex assembly, as assessed by BN-Native PAGE with identical loading of mitochondrial extracts following immune blotting (Figures 3D and S3A). In support of this observation, the enzymatic activity of complex I, III, and IV were also suppressed in *Steap4*^{AKO} iWAT compared to *Steap4*$^{f/f}$ controls (Figure 3E). Consistently, the impact of Steap4 in mitochondrial function was also observed in *ex vivo* differentiated primary adipocytes (Figures S3B–S3E). Taken together, these data suggest that Steap4 plays an important role in maintaining mitochondrial function of adipocyte.

Steap4-mediated alternative splicing events had enriched functions in mitochondria

Besides mitochondrial proteins, Steap4 interactome is also significantly enriched (false discovery rate [FDR] <10%) for proteins related to RNA splicing (Figure 2B; Table S3). Specifically, 22 Steap4 interacting proteins were previously reported to be involved in RNA splicing and spliceosome, including regulatory splicing factors and core splicing factors. Consistently, we observed robust nuclear localization of Steap4 (Figures 2B and S2B). To further confirm these interactions between Steap4 and splicing factors, we validated the interactions of Steap4 with some of these splicing factors via coimmunoprecipitation (coIP) performed in homogenates of iWAT from HFD-fed *Steap4*$^{f/f}$ and *Steap4*^{AKO} mice. As expected, Steap4 successfully coimmunoprecipitated with SRSF6, SF3A1, SF3A2, SF3A3, SF3B1, and PRPF19 in *Steap4*$^{f/f}$ iWAT (Figure 4A). Notably, the expression level of these splicing factors, including the coIP validated ones, are comparable between *Steap4*$^{f/f}$ and *Steap4*^{AKO} mice (Figures 4A and S4A).

The interaction between Steap4 and multiple factors involved in RNA splicing process suggests that Steap4 may play a role in RNA splicing. To test this hypothesis, we analyzed RNA-seq data to seek altered splicing events between *Steap4*$^{f/f}$ and *Steap4*^{AKO} iWAT. Specifically, LeafCutter program were used,[26] which detects differential splicing between sample groups by quantifying and comparing spliced reads (i.e., reads that span an intron) across samples. As a result, 182 genes were identified with significantly altered splicing events (adjusted p value <0.05) in iWAT from HFD-fed *Steap4*^{AKO} mice compared with the control mice. We further applied reverse transcription-polymerase chain reaction (RT-PCR) experiment followed by agarose electrophoresis analysis, and confirmed alternative splicing events of *Pkm*, *Tacc2*, *Abcc9*, *Bin1*, and *Mfn2* (Figures 4B–4E and S4B–S4F). Taken together, these data confirmed the impact of Steap4 on regulating alternative splicing.

Interestingly, gene ontology (GO) enrichment analysis indicated that these genes with alternative splicing events are significantly enriched (FDR <10%) in functions linked to mitochondria, intracellular membranes related to mitochondria, and cytoskeleton structures (Figure 4F; Table S5). The regulation of splicing by Steap4 on these genes may lead to the mis-regulation of their expression or alterations in their protein structures, ultimately impacting mitochondria-related function.

Notably, our investigation has identified SRSF6 as one of the splicing factors interacting with Steap4 (Figure 4A). Previous studies suggested a potential role of SRSF6 in the regulation of mitochondrial function.[27–31] For example, the DRAK2-SRSF6 signaling axis was implicated in the alternative splicing of genes related to mitochondrial function in nonalcoholic fatty liver disease (NAFLD).[31] In our study, while SRSF6 was found to pull down both Steap4 and SF3A1 (a key spliceosome component), the knockout of Steap4 reduced the interaction between SF3A1 and SRSF6. This highlights Steap4's role in regulating the SF3A1-SRSF6 complex, indicating its potential involvement in modulating SRSF6-dependent splicing (Figure 4G).

Furthermore, we found a significant enrichment ($p < 10^{-5}$) between transcripts that are differentially spliced in Steap4 deficiency with those regulated by SRSF6-mediated splicing,[27,28] identifying 34 overlapping genes (Table S6). Interestingly, seven out of these 34 overlapping genes are also downregulated in Steap4 deficiency (adjusted $p < 0.05$) (Table S6). These genes, as well as SRSF6, have been previously linked to mitochondrial function, with similar phenotypes observed in Steap4 KO.[27–35] For example, IMMT/MIC60 is a key factor in the mitochondrial contact site and cristae organizing system (MICOS), where many protein complexes (e.g., ETC) are localized.[32,33] TPM1 has been shown to contribute to mitochondrial distribution and morphology.[34] Reduced PKM1 expression has been linked to deficiencies in mitochondrial respiration and ATP production in failing human and mouse hearts.[35] These findings underscore the potential role of Steap4 in regulating SRSF6-dependent alternative splicing of mitochondrial-related genes.

Brown adipocyte Steap4 maintains thermoregulation via modulating mitochondrial activity

Considering the observed crucial impact of Steap4 on mitochondria, we postulated that depletion of Steap4 in mitochondria-rich thermogenic adipocytes, naming brown and beige adipocytes, may impair thermogenesis via accelerating HFD-induced mitochondrial dysfunction. To test this hypothesis, we generated thermogenic adipocyte-specific Steap4-deficient (*Steap4*^{BKO})

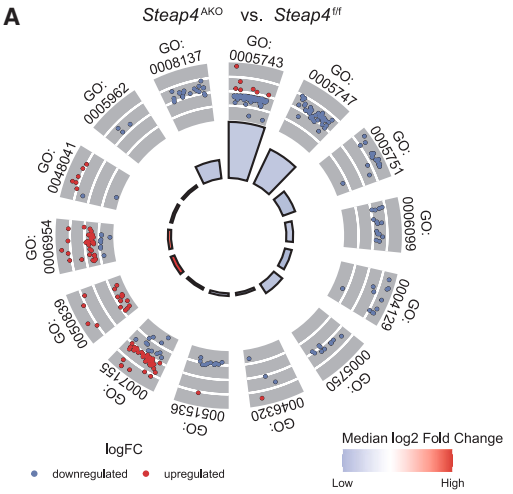

ID	Description
GO:0005743	mitochondrial inner membrane
GO:0005747	mitochondrial respiratory chain complex I
GO:0005751	mitochondrial respiratory chain complex IV
GO:0006099	tricarboxylic acid cycle
GO:0004129	cytochrome–c oxidase activity
GO:0005750	mitochondrial respiratory chain complex III
GO:0046320	regulation of fatty acid oxidation
GO:0051536	iron–sulfur cluster binding
GO:0007155	cell adhesion
GO:0050839	cell adhesion molecule binding
GO:0006954	inflammatory response
GO:0048041	focal adhesion assembly
GO:0005962	mitochondrial isocitrate dehydrogenase complex (NAD+)
GO:0008137	NADH dehydrogenase (ubiquinone) activity

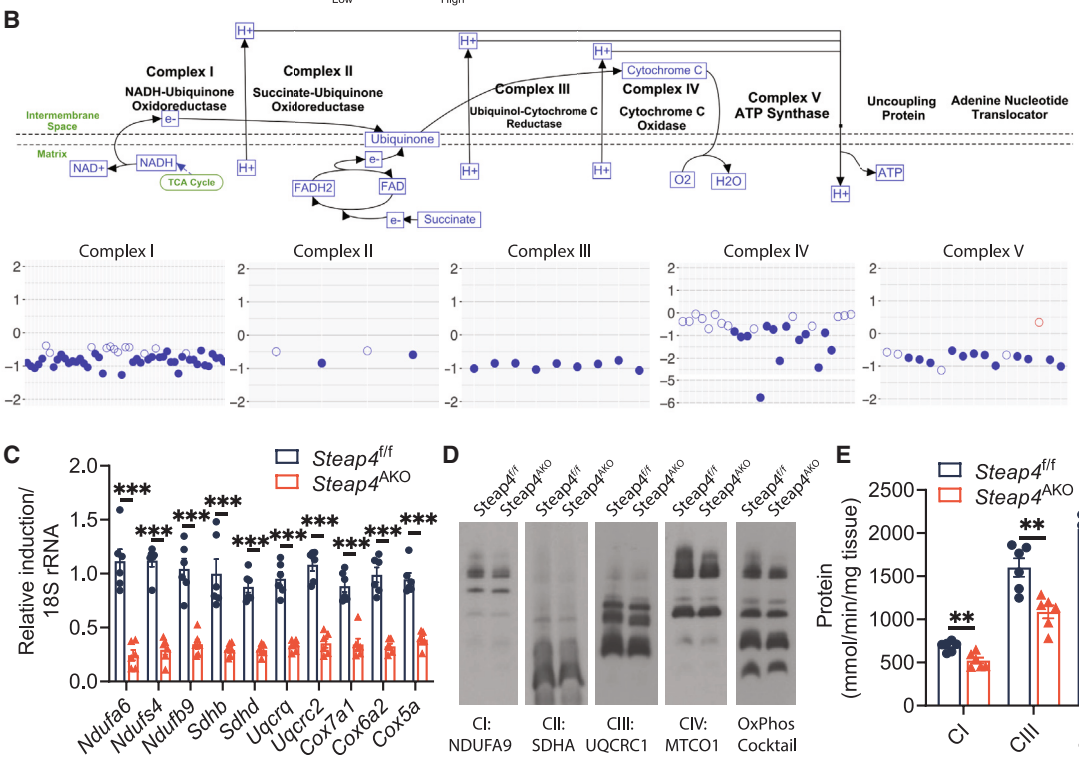

Figure 3. Steap4 deficiency resulted in impaired mitochondrial function in adipocytes

(A) Circular visualization graph shows the selected significant GO terms (FDR <0.1) for differentially expressed genes between iWAT from *Steap4*^{AKO} and *Steap4*$^{f/f}$ HFD-fed mice. Each dot in the outer circle represents an individual upregulated (red) or downregulated (blue) gene. Genes of the same functional term are grouped together, and the description of each group is shown in the right table. The colored bar in the inner circle summarizes the median log2 fold change of the genes sharing the same functional term. The size of the bar represents the significance of each functional term (-$\log_{10}$(FDR)).

(B) Upper: pathway illustration of electron transport chain (ETC) modified based on the Wikipathways database (ID: WP295). Lower: log2 fold change of gene expression between HFD-fed *Steap4*^{AKO} and *Steap4*$^{f/f}$ iWAT. Each dot represents a gene involved in the indicated ETC complex. Blue and red color indicates downregulated and upregulated genes, respectively. Filled dots are statistically significant as assessed by DESeq2 (adjusted *p* value <0.05).

(C) Expression of the indicated mRNAs in iWAT from HFD-fed *Steap4*$^{f/f}$ and *Steap4*^{AKO} mice (n = 6 each group).

(D) Mitochondrial proteins were extracted from iWAT of HFD-fed *Steap4*$^{f/f}$ and *Steap4*^{AKO} mice, identical amounts of protein were loaded and analyzed by BN-PAGE followed by western blot analysis with the indicated antibodies.

(E) Activities of respiratory complexes in the isolated mitochondria from iWAT of HFD-fed *Steap4*$^{f/f}$ and *Steap4*^{AKO} (n = 6 each group).

Statistical significance for all relevant graphs was determined by two-tailed Student's t test. Significance: ** $0.001 \leq p < 0.01$, ***$p < 0.001$. All data represent means ± SEM.

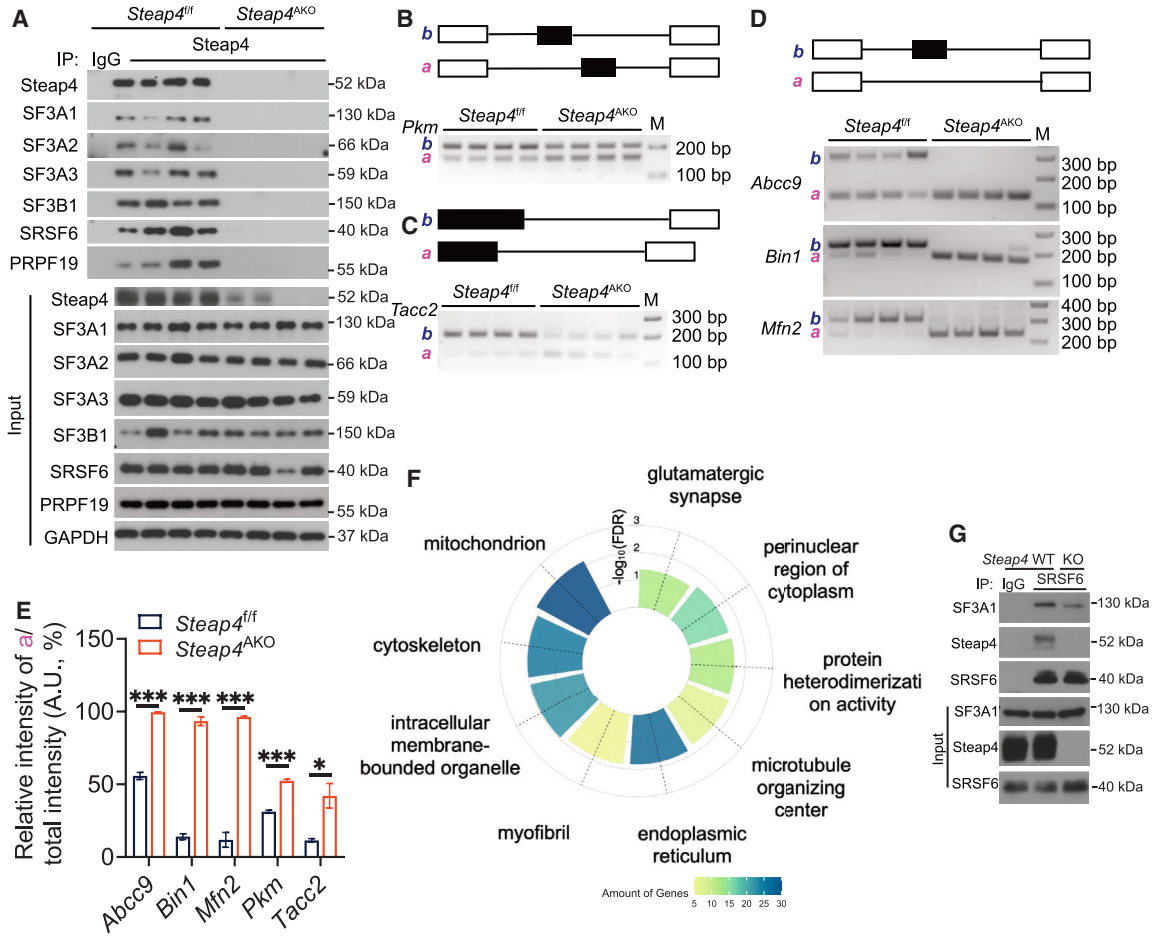

Figure 4. Steap4 regulates RNA alternative splicing of mitochondrial function-related genes in adipose tissue

(A) Co-immunoprecipitation verification of Steap4 interacting proteins in homogenates of iWAT from HFD-fed *Steap4*$^{f/f}$ and *Steap4*^{AKO} mice. Each lane indicates an individual sample.

(B–D) Upper: LeafCutter identified alternative spliced gene patterns as shown in the schematic illustration (Figures S4B-S4F for details). Lower: alternatively spliced events (events *a* vs. *b*) as indicated in the Figure) validated by RT-PCR using RNAs extracted from iWAT of HFD-fed *Steap4*$^{f/f}$ and *Steap4*^{AKO} mice and followed by agarose electrophoresis. Example(s) of mutually exclusive exons (*Pkm*) (B), transcript hosting alternative 5′ splice site (*Tacc2*) (C), and cassette exon (*Abcc9*, *Bin1*, and *Mfn2*) (D), between HFD-fed *Steap4*$^{f/f}$ and *Steap4*^{AKO} iWAT. Each lane in (B)–(D) indicates an individual sample. M: marker.

(E) Quantification of the involvement of event *a* using band intensity measurement as of band *a* to lane total ratios from (B)–(D) by Image Lab software.

Statistical significance was determined by two-tailed Student's t test. $n = 4$ each group. Significance: * $0.01 \leq p < 0.05$, *** $p < 0.001$. All data represent means ± SEM.

(F) Circular visualization graph shows the selected significant GO terms (FDR <0.1) for alternative spliced genes between iWAT from HFD-fed *Steap4*$^{f/f}$ and *Steap4*^{AKO} mice. The size of the colored bar in the inner circle represents the significance of each functional term ($-\log_{10}$(FDR)). The color scale represents the number of identified alternative spliced genes in the indicated functional term.

(G) *Steap4* WT and *Steap4* KO SVFs differentiated on Day6 were subjected to coIP experiment (anti-SRSF6) followed by western blot.

mice by breeding *Steap4*$^{f/f}$ mice to *Ucp1*-Cre transgenic mice (Figures S5A and S5B). Following 12 weeks of HFD feeding, *Steap4*^{BKO} mice exhibited greater weight gain, increased fat mass, and worsened glucose tolerance and insulin sensitivity in *Steap4*^{BKO} mice compared to sex- and age-matched wild-type controls (*Steap4*$^{f/f}$) (Figures 5A–5C). Notably, *Steap4*^{BKO} iBAT showed pronounced lipid accumulation along with suppressed expression of thermogenic genes in response to HFD, including *Ucp1*, *Prdm16*, *Cidea*, *Dio2*, and *Cox8b*, compared with control mice (Figures 5D and 5E). HFD-fed *Steap4*^{BKO} mice also displayed lower body temperatures and showed suppressed VO_2, VCO_2, and energy expenditure in *Steap4*^{BKO} mice, compared with the control mice (Figures 5F and 5G). Interestingly, under mouse thermoneutral conditions (30°C), *Steap4*^{BKO} had already displayed impaired heat dissipation, and the suppressed energy expenditure in *Steap4*^{BKO} was more dramatic under both 22°C and 4°C environmental temperatures compared to *Steap4*$^{f/f}$ controls (Figure 5G). Taken together, these data demonstrate that Steap4 is essential for maintaining brown adipose thermogenesis.

To further investigate the influence of Steap4 on thermogenic adipose tissue, the respiratory capacity was assessed using

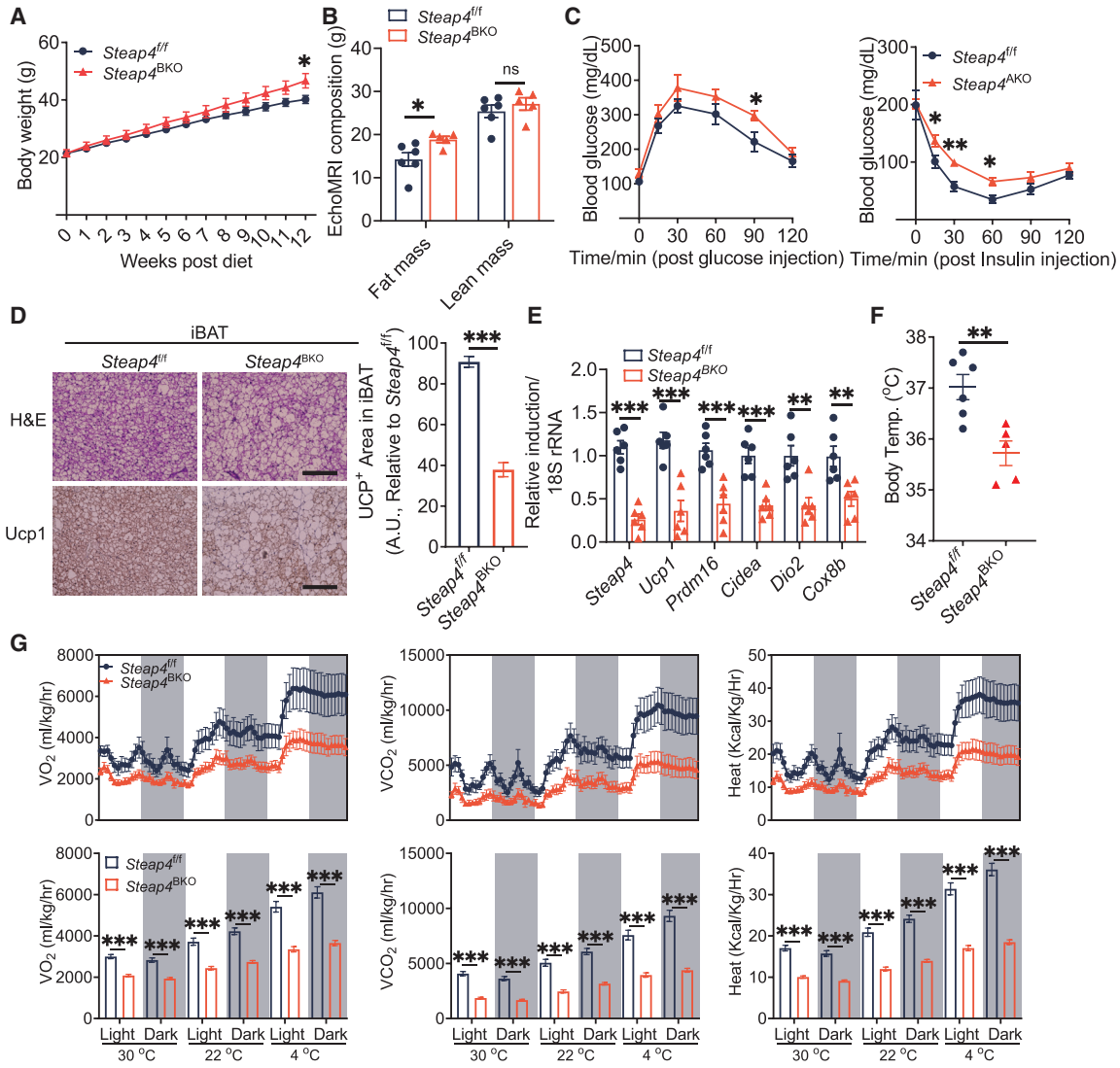

Figure 5. Steap4 deficiency resulted in impaired thermogenesis in brown adipose tissue

(A) Body weight of *Steap4*$^{f/f}$ and *Steap4*^{BKO} mice fed an HFD diet for 12 weeks (n = 6, 5).

(B) EchoMRI analysis of fat mass and lean mass of *Steap4*$^{f/f}$ and *Steap4*^{BKO} mice after HFD feeding (n = 6, 5).

(C) Glucose tolerance test (GTT) and insulin tolerance test (ITT) in HFD-fed *Steap4*$^{f/f}$ and *Steap4*^{BKO} mice (n = 5 pairs).

(D) Left: representative images of H&E staining and Ucp1 staining of iBAT sections from HFD-fed *Steap4*$^{f/f}$ and *Steap4*^{BKO} mice. Right: quantification of Relative Ucp1^{+} area (n = 10 fields). Scale bars: 150 μm.

(E) Expression of the indicated mRNAs in total RNA extractions of iBAT from HFD-fed *Steap4*$^{f/f}$ and *Steap4*^{BKO} mice (n = 6 each group).

(F) Rectal temperatures for HFD-fed *Steap4*$^{f/f}$ and *Steap4*^{BKO} mice (n = 6, 5).

(G) Quantification of VO_2 levels, VCO_2 levels and heat production in HFD-fed *Steap4*$^{f/f}$ and *Steap4*^{BKO} mice (n = 5 pairs), as measured by CLAMS metabolic chambers using indirect calorimetry methods.

Statistical significance for all relevant graphs was determined by two-tailed Student's t test. Significance: * $0.01 \leq p < 0.05$, ** $0.001 \leq p < 0.01$, ***$p < 0.001$. All data represent means ± SEM.

Seahorse analysis in HFD-fed *Steap4*$^{f/f}$ and *Steap4*^{BKO} iBAT explants. As depicted in Figure 6A, the deficiency of Steap4 in brown adipocytes resulted in a marked reduction in both basal and maximal OCR compared to *Steap4*$^{f/f}$ controls. Additionally, the mRNA expression levels of thermogenic genes were also suppressed (Figure 6B). As anticipated, the enzymatic activities mitochondrial ETC complexes was repressed in *Steap4*^{BKO} iBAT (Figure 6C), and supercomplex assembly in *Steap4*^{BKO} iBAT was significantly impaired compared with *Steap4*$^{f/f}$ controls (Figures 6D and S5C), further supporting the modulatory role of Steap4 in mitochondria. Finally, transmission electron microscopy (TEM) analysis revealed a significant decrease in mitochondrial cristae density, indicating mitochondrial structural damage in *Steap4*^{BKO} iBAT compared to the controls (Figures 6E

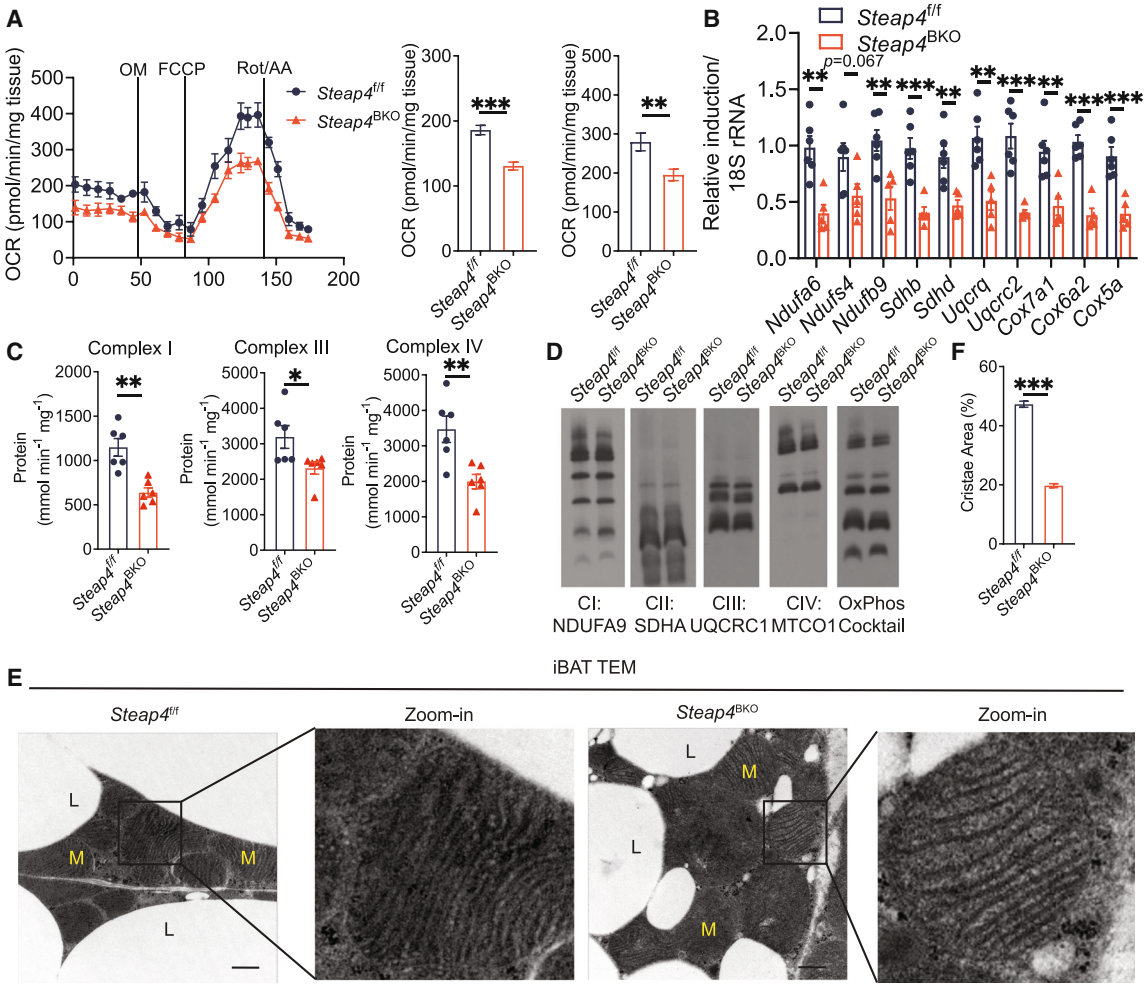

Figure 6. Steap4 deficiency resulted in suppressed mitochondrial function in brown adipose tissue

(A) Left: real-time kinetic rate of oxygen consumption (OCR) of iBAT explants from HFD-fed *Steap4*$^{f/f}$ and *Steap4*^{BKO} mice (n = 5 each group). Right: calculated basal and maximum respiration. OCR levels were normalized to iBAT explant weights.

(B) Expression of the indicated mRNAs in iBAT from HFD-fed *Steap4*$^{f/f}$ and *Steap4*^{BKO} mice (n = 6, 5).

(C) Activities of respiratory complexes in the isolated mitochondria from iBAT of HFD-fed *Steap4*$^{f/f}$ and *Steap4*^{BKO} mice (n = 6 each group).

(D) Mitochondrial proteins were extracted from iBAT of HFD-fed *Steap4*$^{f/f}$ and *Steap4*^{BKO} mice and analyzed by BN-PAGE followed by western blot analysis with the indicated antibodies.

(E) TEM analysis of mitochondrial structure and (F) cristae area quantification in iBAT (n = 20 fields). Scale bars: 0.5 μm. M: mitochondrion, L: lipid droplet.

Statistical significance for all relevant graphs was determined by two-tailed Student's t test. Significance: * $0.01 \leq p < 0.05$, ** $0.001 \leq p < 0.01$, *** $p < 0.001$. All data represent means ± SEM.

and 6F). Overall, these findings demonstrate the indispensable role of Steap4 in maintaining mitochondrial homeostasis and thermogenesis.

DISCUSSION

Adipose metabolism, particularly in the context of obesity, is closely linked to mitochondrial function.[36] Dysfunction in adipose tissue metabolism and mitochondrial activity has been implicated in the progression of obesity, underscoring the importance of understanding the interplay between adipose tissue and mitochondria function.[37,38] Previous research has provided evidence that the expression level of Steap4 in human adipose tissue is associated with adiposity and insulin resistance.[39,40] Similarly, studies conducted in global Steap4 knockout mouse models suggest that Steap4 plays a crucial role in integrating inflammatory and metabolic responses, contributing to systemic metabolic homeostasis.[14] However, it remains unclear whether and how Steap4 impacts adipocytes, especially regarding its role in modulating energy expenditure.

In this study, we generated adipocyte- and thermogenic adipocyte-specific Steap4-deficient mice to investigate the potential effects of Steap4 on obesity induced by HFD. The deficiency of Steap4 in both strains of mice resulted in impaired metabolic function in response to the HFD, characterized by accelerated weight gain, insulin resistance, glucose intolerance.

Importantly, Steap4 deficiency led to adipocyte mitochondrial dysfunction, thereby affecting thermogenesis and energy expenditure.

Our studies demonstrated that Steap4 deficiency in adipose tissue led to suppressed ETC complex activity and impaired supercomplex assembly, suggesting that Steap4 may participate in maintaining mitochondrial function. A previous study indeed showed that gut epithelial cell-specific overexpression of Steap4 increased mitochondrial iron levels in intestinal epithelial cells and oxidative stress, which resulted in experimental colitis and colon cancer in mice.[22] Intriguingly, we found that Steap4 deficiency was able to further reduced ETC complex activities in the presence of iron chelator (as well as copper chelator) (Figure S3E), indicating the role of Steap4 in adipocytes might be beyond the known metalloreductase activity. Although our data cannot exclude the possibility that longer-term consequences of losing Steap4 metalloprotease activity may contribute to the ETC dysfunction observed in Steap4 KO cells, these observations raise the possibility that Steap4 might be involved in additional cellular processes.

Notably, our results revealed a significant enrichment of Steap4 in interacting with splicing factors. Consistently, Steap4 deficiency led to alternative splicing events, with genes harboring these Steap4-mediated splicing changes being significantly enriched in mitochondria. For instance, *Abcc9*, which encodes ATP binding cassette subfamily C member 9 or sulfonylurea receptor 2, was reported to have two isoforms, *Sur2a* and *Sur2b*. Previous study showed that SUR2B exhibits lower ATPase activity than SUR2A.[41] In this study, we observed that *Sur2b* isoform is more enriched in *Steap4*^{AKO} adipose tissue compared to *Steap4*$^{f/f}$ controls, implying that Steap4 may influence ATPase activity by regulating the alternative splicing of *Abcc9*. In addition, it is important to note that our cellular subfractionation and confocal imaging suggested the presence of Steap4 in the nucleus. Taken together, our findings suggest a novel regulatory mechanism by which Steap4 modulates mitochondria function—potentially by regulating the splicing of mitochondria-related genes.

Our mass spectrometry data suggest that Steap4 interacts with the serine/arginine-rich (SR) protein SRSF6, which has been previously implicated in the alternative splicing of genes related to mitochondrial function in multiple studies. We observed a significant enrichment between transcripts differentially spliced in Steap4-deficient cells and those regulated by SRSF6, strongly suggesting that Steap4 and SRSF6 may work together to regulate critical splicing events. To explore this further, we used coIP assays, which confirmed that Steap4 and SRSF6 interact, with each protein able to pull down the other. SR proteins, like SRSF6, play a key role in spliceosome assembly and recruitment, often interacting with core components during the splicing process.[27–31] Indeed, we found that SRSF6 can pull down SF3A1, a core component of the spliceosome. Interestingly, in the absence of Steap4, the interaction between SRSF6 and SF3A1 was significantly reduced, suggesting that Steap4 is involved in regulating the SF3A1-SRSF6 complex. These findings imply a potential regulatory role for Steap4 in SRSF6-dependent splicing events.

We identified several genes whose splicing may be regulated by both SRSF6 and Steap4, and which were significantly downregulated in Steap4-deficient cells. This downregulation is likely driven by alternative splicing regulation, as previously reported.[42–44] Alternative splicing can produce mRNA isoforms with sequences that are recognized by specific RNA-binding proteins or microRNAs, targeting them for degradation by cellular machinery involved in mRNA turnover.[42–44] Additionally, alternative splicing can, in some cases, introduce premature stop codons or alter coding regions, which are often targeted for degradation through mechanisms such as nonsense-mediated decay (NMD), leading to reduced gene expression.[42–44] In Steap4-deficient cells, the alternative splicing for genes likely results in decreased levels of functional proteins, impairing mitochondrial integrity, and energy production. Among these downregulated genes, which are likely regulated by both SRSF6 and Steap4, IMMT/MIC60 and TPM1 are involved in essential mitochondrial functions, such as the mitochondrial contact site and cristae organizing system (MICOS), as well as mitochondrial distribution and morphology.[32–34] Reduced expression of PKM1, another gene in this list, has been linked to impaired mitochondrial respiration and ATP production.[35] This downregulation of critical mitochondrial-related genes correlates with the mitochondrial dysfunction observed in Steap4 knockout models. Additionally, the interactions between Steap4 and other splicing factors present an intriguing opportunity for further exploration. Similar to SF3A1, some of these interactions may belong to the same Steap4/SRSF6 axis, with SR proteins dynamically interacting with the spliceosome at different stages of splicing,[42–48] while others may function independently. Together, these findings support a model in which Steap4 regulates mitochondrial function by modulating alternative splicing events of mitochondria-related genes (e.g., through SRSF6).

In this study, we observed the adipocyte-specific Steap4 deficiency led to impaired mitochondrial function, thermogenesis, and energy expenditure. Besides Steap4's involvement in regulating splicing, we also found that Steap4 interacts with a set of mitochondrial function-related proteins, suggesting that Steap4 might modulate adipocyte mitochondrial function via its interactions with these mitochondrial proteins. These findings highlight the significance of Steap4 in regulating mitochondrial activity and thermogenic capacity in BAT, which has emerged as a potential therapeutic target for combating obesity. By enhancing brown adipocyte function and promoting thermogenesis, excess energy stored as WAT can be burned, leading to a reduction in overall body weight and improved metabolic health.[49] The impairment in mitochondrial function and thermogenesis in Steap4-deficient adipocytes indicates the essential role of Steap4 in the regulation of BAT function, implicating Steap4 as a potential target to boost thermogenic capacity in combatting obesity.

In summary, our study has revealed a new structural role of Steap4 that extends beyond its well-documented metalloreductase activity. We found that Steap4 is involved in maintaining adipocyte homeostasis and promoting thermogenesis through its modulation of mitochondrial function and participates in the alternative splicing of mitochondrial-related genes. These

findings indicate that Steap4 may play a putative protective role in the context of obesity development, presenting potential therapeutic targets for obesity treatment.

Limitations of the study

While we demonstrated that Steap4 selectively affects mitochondrial genes through interactions with splicing factors, including SRSF6-containing complexes, the precise mechanisms of its role in dynamic splicing regulation in adipocytes remain unclear. Steap4 deficiency reduced ETC complex activities in the presence of chelators, suggesting roles beyond metalloreductase activity. Further analysis using the catalytic mutant is needed to gain clearer mechanistic insights. Additionally, studies are required to elucidate further whether Steap4's nuclear translocation and mitochondrial localization are interconnected regulatory processes in adipocytes.

RESOURCE AVAILABILITY

Lead contact

Further information and requests for resources should be directed to and will be fulfilled by the lead contact Xiao Li (xiao.li9@case.edu).

Materials availability

This study did not generate new unique reagents.

Data and code availability

- The RNA sequencing data generated in this study have been deposited in the NCBI's Gene Expression Omnibus (GEO) database. The mass spectrometry proteomics data have been deposited to the ProteomeXchange Consortium via the PRIDE partner repository. This paper analyzes existing data from previous publications. Links to these publications/resources, as well as the data generated in this study, are listed in the key resources table.
- This paper does not report original code.
- Any additional information required to reanalyze the data reported in this work paper is available from the lead contact upon request.

ACKNOWLEDGMENTS

We thank Ms. Mei Yin from the Cleveland Clinic Imaging Core for her tremendous assistance in past and current studies. This work was supported by Case Western Reserve University through departmental start-up funding and the High-Performance Computing award: both awarded to X.L., and National Institutes of Health shared instrument grant S10OD030398 to B.W. We also acknowledge the assistance of the Case Western Reserve University School of Medicine Light Microscopy Imaging Facility and support by NIH grant #S10OD02499601.

AUTHOR CONTRIBUTIONS

Conceptualization, Xiao Li, Xiaoxia Li, and H.W.; methodology, Xiao Li, H.W., L.Z., X.C., B.W., L.H., J.Z., W.Q., Xiaoxia Li, and K.B.; investigation, Xiao Li, H.W., L.Z., X.C, L.H., J.Z., Xiaoxia Li, and K.B.; writing – original draft, Xiao Li, H.W., and L.Z.; writing – review and editing, Xiao Li, L.Z., and X.C.; visualization, Xiao Li, H.W.,L.Z., and X.C.; supervision, Xiao Li; project administration, Xiao Li; funding acquisition, Xiao Li.

DECLARATION OF INTERESTS

The authors declare no competing interests.

STAR★METHODS

Detailed methods are provided in the online version of this paper and include the following:

- KEY RESOURCES TABLE
- EXPERIMENTAL MODEL AND STUDY PARTICIPANT DETAILS
  - Animals and animal care statement
  - Primary mouse stromal vascular fraction cells (SVFs) and differentiation
- METHOD DETAILS
  - Glucose tolerance test (GTT), insulin tolerance test (ITT), and body temperature measurement
  - Indirect calorimetry analysis and EchoMRI
  - Real-time analysis of OCR
  - Co-immunoprecipitation and immunoblot based analysis
  - Immunohistochemistry (IHC) and immunocytochemistry (ICC)
  - Mitochondrial isolation and blue native polyacrylamide gel electrophoresis (BN-PAGE)
  - Nuclei isolation
  - Real-time qPCR
  - Transmission electron microscopy
  - Proteomic analysis of Steap4-interacting proteins
  - Subcellular localization analysis
  - RNA-seq analysis
  - Gene Ontology enrichment analysis and visualization
  - Differential splicing analysis
  - Validation of differential splice events from LeafCutter
  - Spectrophotometric assays of mitochondrial respiratory complex activity
- QUANTIFICATION AND STATISTICAL ANALYSIS

SUPPLEMENTAL INFORMATION

Supplemental information can be found online at https://doi.org/10.1016/j.isci.2025.111903.

Received: January 22, 2024
Revised: November 21, 2024
Accepted: January 22, 2025
Published: January 25, 2025

REFERENCES

1. Ng, M., Fleming, T., Robinson, M., Thomson, B., Graetz, N., Margono, C., Mullany, E.C., Biryukov, S., Abbafati, C., Abera, S.F., et al. (2014). Global, regional, and national prevalence of overweight and obesity in children and adults during 1980–2013: a systematic analysis for the Global Burden of Disease Study. Lancet *384*, 766–781. https://doi.org/10.1016/S0140-6736(14)60460-8.
2. Hajer, G.R., van Haeften, T.W., and Visseren, F.L.J. (2008). Adipose tissue dysfunction in obesity, diabetes, and vascular diseases. Eur. Heart J. *29*, 2959–2971. https://doi.org/10.1093/eurheartj/ehn387.
3. Longo, M., Zatterale, F., Naderi, J., Parrillo, L., Formisano, P., Raciti, G.A., Beguinot, F., and Miele, C. (2019). Adipose Tissue Dysfunction as Determinant of Obesity-Associated Metabolic Complications. Int. J. Mol. Sci. *20*, 2358. https://doi.org/10.3390/ijms20092358.
4. Zhang, F., Hao, G., Shao, M., Nham, K., An, Y., Wang, Q., Zhu, Y., Kusminski, C.M., Hassan, G., Gupta, R.K., et al. (2018). An adipose tissue atlas: an image-guided identification of human-like BAT and beige depots in rodents. Cell Metabol. *27*, 252–262. https://doi.org/10.1016/j.cmet.2017.12.004.
5. Cypess, A.M., Lehman, S., Williams, G., Tal, I., Rodman, D., Goldfine, A.B., Kuo, F.C., Palmer, E.L., Tseng, Y.H., Doria, A., et al. (2009). Identification and importance of brown adipose tissue in adult humans. N. Engl. J. Med. *360*, 1509–1517. https://doi.org/10.1056/NEJMoa0810780.

6. Bournat, J.C., and Brown, C.W. (2010). Mitochondrial dysfunction in obesity. Curr. Opin. Endocrinol. Diabetes Obes. *17*, 446–452. https://doi.org/10.1097/MED.0b013e32833c3026.

7. Zhu, Q., An, Y.A., and Scherer, P.E. (2022). Mitochondrial regulation and white adipose tissue homeostasis. Trends Cell Biol. *32*, 351–364. https://doi.org/10.1016/j.tcb.2021.10.008.

8. Bjorndal, B., Burri, L., Staalesen, V., Skorve, J., and Berge, R.K. (2011). Different Adipose Depots: Their Role in the Development of Metabolic Syndrome and Mitochondrial Response to Hypolipidemic Agents. J. Obes. *2011*, 490650. https://doi.org/10.1155/2011/490650.

9. Kotzbeck, P., Giordano, A., Mondini, E., Murano, I., Severi, I., Venema, W., Cecchini, M.P., Kershaw, E.E., Barbatelli, G., Haemmerle, G., et al. (2018). Brown adipose tissue whitening leads to brown adipocyte death and adipose tissue inflammation. J. Lipid Res. *59*, 784–794. https://doi.org/10.1194/jlr.M079665.

10. Becher, T., Palanisamy, S., Kramer, D.J., Eljalby, M., Marx, S.J., Wibmer, A.G., Butler, S.D., Jiang, C.S., Vaughan, R., Schöder, H., et al. (2021). Brown adipose tissue is associated with cardiometabolic health. Nat. Med. *27*, 58–65. https://doi.org/10.1038/s41591-020-1126-7.

11. Ouellet, V., Routhier-Labadie, A., Bellemare, W., Lakhal-Chaieb, L., Turcotte, E., Carpentier, A.C., and Richard, D. (2011). Outdoor Temperature, Age, Sex, Body Mass Index, and Diabetic Status Determine the Prevalence, Mass, and Glucose-Uptake Activity of 18F-FDG-Detected BAT in. J. Clin. Endocrinol. Metab. *96*, 192–199. https://doi.org/10.1210/jc.2010-0989.

12. Lee, P., Greenfield, J.R., Ho, K.K.Y., and Fulham, M.J. (2010). A critical appraisal of the prevalence and metabolic significance of brown adipose tissue in adult humans. Am. J. Physiol. Endocrinol. Metab. *299*, E601–E606. https://doi.org/10.1152/ajpendo.00298.2010.

13. Wang, Q., Zhang, M., Xu, M., Gu, W., Xi, Y., Qi, L., Li, B., and Wang, W. (2015). Brown adipose tissue activation is inversely related to central obesity and metabolic parameters in adult human. PLoS One *10*, e0123795. https://doi.org/10.1371/journal.pone.0123795.

14. Wellen, K.E., Fucho, R., Gregor, M.F., Furuhashi, M., Morgan, C., Lindstad, T., Vaillancourt, E., Gorgun, C.Z., Saatcioglu, F., and Hotamisligil, G.S. (2007). Coordinated regulation of nutrient and inflammatory responses by STAMP2 is essential for metabolic homeostasis. Cell *129*, 537–548.

15. Kim, H.Y., Park, S.Y., Lee, M.H., Rho, J.H., Oh, Y.J., Jung, H.U., Yoo, S.H., Jeong, N.Y., Lee, H.J., Suh, S., et al. (2015). Hepatic STAMP2 alleviates high fat diet-induced hepatic steatosis and insulin resistance. J. Hepatol. *63*, 477–485. https://doi.org/10.1016/j.jhep.2015.01.025.

16. ten Freyhaus, H., Calay, E.S., Yalcin, A., Vallerie, S.N., Yang, L., Calay, Z.Z., Saatcioglu, F., and Hotamisligil, G.S. (2012). Stamp2 controls macrophage inflammation through nicotinamide adenine dinucleotide phosphate homeostasis and protects against atherosclerosis. Cell Metabol. *16*, 81–89. https://doi.org/10.1016/j.cmet.2012.05.009.

17. Kim, H.Y., Cho, H.K., Yoo, S.K., and Cheong, J.H. (2012). Hepatic STAMP2 decreases hepatitis B virus X protein-associated metabolic deregulation. Exp. Mol. Med. *44*, 622–632. https://doi.org/10.3858/emm.2012.44.10.071.

18. Consortium, T.G., Ardlie, K.G., Deluca, D.S., Segrè, A.V., Sullivan, T.J., Young, T.R., Gelfand, E.T., Trowbridge, C.A., Maller, J.B., Tukiainen, T., et al. (2015). The Genotype-Tissue Expression (GTEx) pilot analysis: Multitissue gene regulation in humans. Science *348*, 648–660. https://doi.org/10.1126/science.1262110.

19. Binder, J.X., Pletscher-Frankild, S., Tsafou, K., Stolte, C., O'Donoghue, S.I., Schneider, R., and Jensen, L.J. (2014). COMPARTMENTS: unification and visualization of protein subcellular localization evidence. Database *2014*, bau012.

20. Rath, S., Sharma, R., Gupta, R., Ast, T., Chan, C., Durham, T.J., Goodman, R.P., Grabarek, Z., Haas, M.E., Hung, W.H.W., et al. (2021). MitoCarta3.0: an updated mitochondrial proteome now with sub-organelle localization and pathway annotations. Nucleic Acids Res. *49*, D1541–D1547. https://doi.org/10.1093/nar/gkaa1011.

21. Morgenstern, M., Peikert, C.D., Lubbert, P., Suppanz, I., Klemm, C., Alka, O., Steiert, C., Naumenko, N., Schendzielorz, A., Melchionda, L., et al. (2021). Quantitative high-confidence human mitochondrial proteome and its dynamics in cellular context. Cell Metabol. *33*, 2464–2483. https://doi.org/10.1016/j.cmet.2021.11.001.

22. Xue, X., Bredell, B.X., Anderson, E.R., Martin, A., Mays, C., Nagao-Kitamoto, H., Huang, S., Győrffy, B., Greenson, J.K., Hardiman, K., et al. (2017). Quantitative proteomics identifies STEAP4 as a critical regulator of mitochondrial dysfunction linking inflammation and colon cancer. Proc. Natl. Acad. Sci. USA *114*, E9608–E9617.

23. Jastroch, M., Divakaruni, A.S., Mookerjee, S., Treberg, J.R., and Brand, M.D. (2010). Mitochondrial proton and electron leaks. Essays Biochem. *47*, 53–67. https://doi.org/10.1042/bse0470053.

24. Letts, J.A., and Sazanov, L.A. (2017). Clarifying the supercomplex: the higher-order organization of the mitochondrial electron transport chain. Nat. Struct. Mol. Biol. *24*, 800–808. https://doi.org/10.1038/nsmb.3460.

25. Acin-Perez, R., Fernandez-Silva, P., Peleato, M.L., Perez-Martos, A., and Enriquez, J.A. (2008). Respiratory active mitochondrial supercomplexes. Mol. Cell *32*, 529–539. https://doi.org/10.1016/j.molcel.2008.10.021.

26. Li, Y.I., Knowles, D.A., Humphrey, J., Barbeira, A.N., Dickinson, S.P., Im, H.K., and Pritchard, J.K. (2018). Annotation-free quantification of RNA splicing using LeafCutter. Nat. Genet. *50*, 151–158. https://doi.org/10.1038/s41588-017-0004-9.

27. Wagner, A.R., Scott, H.M., West, K.O., Vail, K.J., Fitzsimons, T.C., Coleman, A.K., Carter, K.E., Watson, R.O., and Patrick, K.L. (2021). Global Transcriptomics Uncovers Distinct Contributions From Splicing Regulatory Proteins to the Macrophage Innate Immune Response. Front. Immunol. *12*, 656885. https://doi.org/10.3389/fimmu.2021.656885.

28. Wagner, A.R., Weindel, C.G., West, K.O., Scott, H.M., Watson, R.O., and Patrick, K.L. (2022). SRSF6 balances mitochondrial-driven innate immune outcomes through alternative splicing of BAX. Elife *11*, e82244. https://doi.org/10.7554/eLife.82244.

29. Lin, J.C., Chi, Y.L., Peng, H.Y., and Lu, Y.H. (2016). RBM4-Nova1-SRSF6 splicing cascade modulates the development of brown adipocytes. Biochim. Biophys. Acta *1859*, 1368–1379. https://doi.org/10.1016/j.bbagrm.2016.08.006.

30. Juan-Mateu, J., Alvelos, M.I., Turatsinze, J.V., Villate, O., Lizarraga-Mollinedo, E., Grieco, F.A., Marroquí, L., Bugliani, M., Marchetti, P., and Eizirik, D.L. (2018). SRp55 Regulates a Splicing Network That Controls Human Pancreatic beta-Cell Function and Survival. Diabetes *67*, 423–436. https://doi.org/10.2337/db17-0736.

31. Li, Y., Xu, J., Lu, Y., Bian, H., Yang, L., Wu, H., Zhang, X., Zhang, B., Xiong, M., Chang, Y., et al. (2021). DRAK2 aggravates nonalcoholic fatty liver disease progression through SRSF6-associated RNA alternative splicing. Cell Metabol. *33*, 2004–2020. https://doi.org/10.1016/j.cmet.2021.09.008.

32. Li, H., Ruan, Y., Zhang, K., Jian, F., Hu, C., Miao, L., Gong, L., Sun, L., Zhang, X., Chen, S., et al. (2016). Mic60/Mitofilin determines MICOS assembly essential for mitochondrial dynamics and mtDNA nucleoid organization. Cell Death Differ. *23*, 380–392. https://doi.org/10.1038/cdd.2015.102.

33. Tsai, P.I., Lin, C.H., Hsieh, C.H., Papakyrikos, A.M., Kim, M.J., Napolioni, V., Schoor, C., Couthouis, J., Wu, R.M., Wszolek, Z.K., et al. (2018). PINK1 Phosphorylates MIC60/Mitofilin to Control Structural Plasticity of Mitochondrial Crista Junctions. Mol. Cell *69*, 744–756. https://doi.org/10.1016/j.molcel.2018.01.026.

34. Simon, V.R., Karmon, S.L., and Pon, L.A. (1997). Mitochondrial inheritance: cell cycle and actin cable dependence of polarized mitochondrial movements in Saccharomyces cerevisiae. Cell Motil Cytoskeleton *37*, 199–210. https://doi.org/10.1002/(SICI)1097-0169(1997)37:3<199::AID-CM2>3.0.CO;2.

35. Li, Q., Li, C., Elnwasany, A., Sharma, G., An, Y.A., Zhang, G., Elhelaly, W.M., Lin, J., Gong, Y., Chen, G., et al. (2021). PKM1 Exerts Critical Roles in Cardiac Remodeling Under Pressure Overload in the Heart. Circulation *144*, 712–727. https://doi.org/10.1161/CIRCULATIONAHA.121.054885.

36. Joffin, N., Paschoal, V.A., Gliniak, C.M., Crewe, C., Elnwasany, A., Szweda, L.I., Zhang, Q., Hepler, C., Kusminski, C.M., Gordillo, R., et al. (2021). Mitochondrial metabolism is a key regulator of the fibro-inflammatory and adipogenic stromal subpopulations in white adipose tissue. Cell Stem Cell *28*, 702–717. https://doi.org/10.1016/j.stem.2021.01.002.

37. Lowell, B.B., and Shulman, G.I. (2005). Mitochondrial dysfunction and type 2 diabetes. Science *307*, 384–387.

38. Prasun, P. (2020). Mitochondrial dysfunction in metabolic syndrome. Biochim. Biophys. Acta, Mol. Basis Dis. *1866*, 165838.

39. Arner, P., Stenson, B.M., Dungner, E., Näslund, E., Hoffstedt, J., Ryden, M., and Dahlman, I. (2008). Expression of Six Transmembrane Protein of Prostate 2 in Human Adipose Tissue Associates with Adiposity and Insulin Resistance. J. Clin. Endocrinol. Metab. *93*, 2249–2254. https://doi.org/10.1210/jc.2008-0206.

40. Zhang, C.M., Chi, X., Wang, B., Zhang, M., Ni, Y.H., Chen, R.H., Li, X.N., and Guo, X.R. (2008). Downregulation of STEAP4, a highly-expressed TNF-α αα α-inducible gene in adipose tissue, is associated with obesity in humans. Acta Pharmacol. Sin. *29*, 587–592. https://doi.org/10.1111/j.1745-7254.2008.00793.x.

41. de Wet, H., Fotinou, C., Amad, N., Dreger, M., and Ashcroft, F.M. (2010). The ATPase activities of sulfonylurea receptor 2A and sulfonylurea receptor 2B are influenced by the C-terminal 42 amino acids. FEBS J. *277*, 2654–2662. https://doi.org/10.1111/j.1742-464X.2010.07675.x.

42. Baralle, F.E., and Giudice, J. (2017). Alternative splicing as a regulator of development and tissue identity. Nat. Rev. Mol. Cell Biol. *18*, 437–451. https://doi.org/10.1038/nrm.2017.27.

43. Rogalska, M.E., Vivori, C., and Valcárcel, J. (2023). Regulation of pre-mRNA splicing: roles in physiology and disease, and therapeutic prospects. Nat. Rev. Genet. *24*, 251–269. https://doi.org/10.1038/s41576-022-00556-8.

44. Marasco, L.E., and Kornblihtt, A.R. (2023). The physiology of alternative splicing. Nat. Rev. Mol. Cell Biol. *24*, 242–254. https://doi.org/10.1038/s41580-022-00545-z.

45. Jeong, S. (2017). SR Proteins: Binders, Regulators, and Connectors of RNA. Mol. Cell. *40*, 1–9. https://doi.org/10.14348/molcells.2017.2319.

46. Howard, J.M., and Sanford, J.R. (2015). The RNAissance family: SR proteins as multifaceted regulators of gene expression. Wiley Interdiscip. Rev. RNA *6*, 93–110. https://doi.org/10.1002/wrna.1260.

47. Shepard, P.J., and Hertel, K.J. (2009). The SR protein family. Genome Biol. *10*, 242. https://doi.org/10.1186/gb-2009-10-10-242.

48. Manley, J.L., and Krainer, A.R. (2010). A rational nomenclature for serine/arginine-rich protein splicing factors (SR proteins). Genes Dev. *24*, 1073–1074. https://doi.org/10.1101/gad.1934910.

49. Nedergaard, J., and Cannon, B. (2010). The changed metabolic world with human brown adipose tissue: therapeutic visions. Cell Metabol. *11*, 268–272. https://doi.org/10.1016/j.cmet.2010.03.007.

50. Liao, Y., Zhao, J., Bulek, K., Tang, F., Chen, X., Cai, G., Jia, S., Fox, P.L., Huang, E., Pizarro, T.T., et al. (2020). Inflammation mobilizes copper metabolism to promote colon tumorigenesis via an IL-17-STEAP4-XIAP axis. Nat. Commun. *11*, 900.

51. Eguchi, J., Wang, X., Yu, S., Kershaw, E.E., Chiu, P.C., Dushay, J., Estall, J.L., Klein, U., Maratos-Flier, E., and Rosen, E.D. (2011). Transcriptional control of adipose lipid handling by IRF4. Cell Metabol. *13*, 249–259. https://doi.org/10.1016/j.cmet.2011.02.005.

52. Kong, X., Banks, A., Liu, T., Kazak, L., Rao, R.R., Cohen, P., Wang, X., Yu, S., Lo, J.C., Tseng, Y.H., et al. (2014). IRF4 is a key thermogenic transcriptional partner of PGC-1alpha. Cell *158*, 69–83. https://doi.org/10.1016/j.cell.2014.04.049.

53. Pettersson, U.S., Waldén, T.B., Carlsson, P.O., Jansson, L., and Phillipson, M. (2012). Female mice are protected against high-fat diet induced metabolic syndrome and increase the regulatory T cell population in adipose tissue. PLoS One *7*, e46057. https://doi.org/10.1371/journal.pone.0046057.

54. Bugge, A., Dib, L., and Collins, S. (2014). Measuring respiratory activity of adipocytes and adipose tissues in real time. In Methods in enzymology, O.A. MacDougald, ed. (Elsevier), pp. 233–247.

55. DeCaprio, J., and Kohl, T.O. (2019). Cross-Linking Antibodies to Beads Using Dimethyl Pimelimidate (DMP). Cold Spring Harb. Protoc. *2019*, pdb-rot098624. https://doi.org/10.1101/pdb.prot098624.

56. Frezza, C., Cipolat, S., and Scorrano, L. (2007). Organelle isolation: functional mitochondria from mouse liver, muscle and cultured filroblasts. Nat. Protoc. *2*, 287–295.

57. Thul, P.J., Akesson, L., Wiking, M., Mahdessian, D., Geladaki, A., Ait Blal, H., Alm, T., Asplund, A., Bjork, L., Breckels, L.M., et al. (2017). A subcellular map of the human proteome. Science *356*, eaal3321. https://doi.org/10.1126/science.aal3321.

58. Yeh, S.T., Lee, H.L., Aune, S.E., Chen, C.L., Chen, Y.R., and Angelos, M.G. (2009). Preservation of mitochondrial function with cardiopulmonary resuscitation in prolonged cardiac arrest in rats. J. Mol. Cell. Cardiol. *47*, 789–797. https://doi.org/10.1016/j.yjmcc.2009.09.003.

59. Han, Z., Chen, Y.R., Jones, C.I., 3rd, Meenakshisundaram, G., Zweier, J.L., and Alevriadou, B.R. (2007). Shear-induced reactive nitrogen species inhibit mitochondrial respiratory complex activities in cultured vascular endothelial cells. Am. J. Physiol. Cell Physiol. *292*, C1103–C1112. https://doi.org/10.1152/ajpcell.00389.2006.

STAR★METHODS

KEY RESOURCES TABLE

REAGENT or RESOURCE	SOURCE	IDENTIFIER
Antibodies		
Anti-Steap4	ProteinTech	Cat# 11944-1-AP; RRID:AB_2197868
Anti-SF3A1	ProteinTech	Cat# 15858-1-AP;RRID:AB_2186354
Anti-SF3A2	ProteinTech	Cat# 15596-1-AP; RRID:AB_2301609
Anti-SF3A3	ProteinTech	Cat# 12070-1-AP; RRID:AB_2186372
Anti-SRSF6	ProteinTech	Cat# 11772-1-AP; RRID:AB_2185212
Anti-SRSF6/SRp55 (for IP)	Santa Cruz	Cat# sc-57954; RRID:AB_785899
Anti-PRPF19	ProteinTech	Cat# 15414-1-AP; RRID:AB_10637855
Anti-β-Actin	Cell Signaling	Cat# 3700; RRID:AB_2242334
Anti-ACO2	Cell Signaling	Cat# 6922; RRID:AB_10828218
Anti-CYP1B1	ProteinTech	Cat# 18505-1-AP; RRID:AB_2878548
Anti-VDAC	Abcam	Cat# ab154856; RRID:AB_2687466
Anti-GAPDH	Cell Signaling	Cat# 97166; RRID:AB_2756824
Goat Anti-Mouse IgG(HRP Conjugate)	JacksonImmuno Research	Cat# 115-035-003; RRID:AB_10015289
Goat Anti-Rabbit IgG(HRP Conjugate)	JacksonImmuno Research	Cat# 111-035-003; RRID:AB_2313567
Mouse Anti-rabbit IgG(HRP Conjugate) (conformation specific)	Cell Signaling	Cat# 5127s; RRID:AB_10892860
Rabbit Anti-Mouse IgG(HRP Conjugate) (Light Chain Specific)	Cell Signaling	Cat# 58802s; RRID:AB_2799549
Mouse Anti-Rabbit IgG(HRP Conjugate) (Light-Chain Specific)	Cell Signaling	Cat# 93702s; RRID:AB_2800208
Anti-total OxPhos	Abcam	Cat# ab110413; RRID:AB_2629281
Anti-NDUFA9	Abcam	Cat# ab14713; RRID:AB_301431
Anti-SDHA	Abcam	Cat# ab14715; RRID:AB_301433
Anti-Ubiquinol-Cytochrome C Reductase Core Protein I	Abcam	Cat# ab110252; RRID:AB_10863633
Anti-MTCO1	Abcam	Cat# ab14705; RRID:AB_2084810
Anti-Tom20	Santa Cruz	Cat# sc-11415; RRID:AB_2207533
Donkey anti-Rabbit IgG, Alexa Fluo 568	Thermo Fisher Scientific	Cat# A10042; RRID:AB_2534017
Anti-Lamin A/C	Santa Cruz	Cat# sc-376248;RRID:AB_10991536
Anti-Mac2	Cedarlane	Cat# CL8942AP; RRID:AB_10060357
anti-UCP1	Abcam	Cat# ab261912
Chemicals, peptides, and recombinant proteins		
Bathocuproine disulfonic acid	Millipore Sigma	146625
Deferoxamine	Millipore Sigma	D9533
SYBR Green Real-Time PCR Master Mix	Applied Biosystems	4309155
SuperScript II Reverse Transcriptase	Thermo Fisher Scientific	18064022
KOD Hot Start DNA Polymerase	Millipore Sigma	71086
3-Isobutyl-1-methylxanthine	Millipore Sigma	I5879
Rosiglitazone	Millipore Sigma	R2408
Dexamethasone	Millipore Sigma	D4902
Collagenase D	Millipore Sigma(Roche)	11088882001&11088866001
Dimethyl pimelimidate (DMP)	Thermo Fisher Scientific	21667
ProLong Gold Antifade Reagent with DAPI	Thermo Fisher Scientific	P36931
Blotting-Grade Blocker	Bio-rad	1706404

(*Continued on next page*)

Continued

REAGENT or RESOURCE	SOURCE	IDENTIFIER
Critical commercial assays		
Nuclear Isolation Kit	Millipore Sigma	NUC101
NativePAGE Novex Bis-Tris Gels	Invitrogen	BN1001BOX
RNeasy Lipid Tissue Mini Kit	Qiagen	74804
Seahorse XFe24 Islet Capture Microplates	Agilent	103518-100
DAB substrate kit	BD Pharmingen	550880
BCA assay Kit	Thermo Fisher Scientific	23227
Deposited data		
RNA sequencing data	This paper	GEO: GSE247291
Mass spectrometry proteomics data	This paper	PRIDE: PXD046997
Genotype-Tissue Expression (GTEx, Release V10)	GTEx Portal, Release V10 (dbGaP Accession phs000424.v10.p2)	https://www.gtexportal.org/home/
MitoCarta3.0: Mouse Mitochondrial proteome	Rath et al.[20]	https://doi.org/10.1093/nar/gkaa1011
MitoCoP: Human mitochondrial high-confidence proteome data	Morgenstern et al.[21]	https://doi.org/10.1016/j.cmet.2021.11.001
COMPARTMENTS: Subcellular localization database	Binder et al.[19]	https://doi.org/10.1093/database/bau012
The Human Protein Atlas	Human Protein Atlas proteinatlas.org	https://www.proteinatlas.org/humanproteome/subcellular
SRSF6-mediated alternative splicing data from the previously published studies	Wagner et al.[27,28]	https://doi.org/10.3389/fimmu.2021.656885 and https://doi.org/10.7554/eLife.82244
WikiPathways: Electron transport chain, Mus musculus (WP295)	WikiPathways	https://www.wikipathways.org/pathways/WP295.html
Experimental models: Cell lines		
Primary mouse stromal vascular fraction cells (SVFs)	This paper	N/A
Experimental models: Organisms/strains		
Mouse: Adiponectin(Adipoq)-Cre	Jackson Labs	028020
Mouse: Ucp1-Cre	Jackson Labs	024670
Mouse: Steap4 flox/flox	Liao et al.[50]	N/A
Oligonucleotides		
Primer sequences for real-time qPCR analyses	This paper	Table S7
Primer sequences for RT-PCR analyses	This paper	Table S8
Software and algorithms		
BioMart 2.52.0 (R package)	Ensembl	https://useast.ensembl.org/info/data/biomart/index.html
DESeq2 1.12.4 (R package)	R Bioconductor	https://www.bioconductor.org/packages/release/bioc/html/DESeq2.html
Database for Annotation, Visualization, and Integrated Discovery (DAVID): Functional Annotation Tool	National Institutes of Health	https://davidbioinformatics.nih.gov/summary.jsp
GraphPad Prism 9	Dotmatics/GraphPad Software	https://www.graphpad.com/
GOPlot 1.0.2 (R package)	GitHub	https://wencke.github.io/
ImageJ Software	National Institutes of Health	https://imagej.net/ij/
Image Lab 6.1 Software	Bio-Rad	https://www.bio-rad.com/en-us/product/image-lab-software
LeafCutter 0.2.9 (R package)	GitHub	https://github.com/davidaknowles/leafcutter/
R version 4.2.0	R Core Team	https://www.r-project.org/
RSEM 1.3.3	GitHub	https://github.com/deweylab/RSEM
STAR 2.7.0	GitHub	https://github.com/alexdobin/STAR
Samtools 1.8	GitHub	https://github.com/samtools
stats function fisher.test 4.2.1(R package)	GitHub	https://github.com/SurajGupta/r-source/tree/master/src/library/stats

(*Continued on next page*)

Continued		
REAGENT or RESOURCE	SOURCE	IDENTIFIER
tidyverse 2.0.0(R package)	GitHub	https://github.com/tidyverse
Other		
High fat diet(60%)	Envigo/ResearchDiet	TD06414/ D12492i

EXPERIMENTAL MODEL AND STUDY PARTICIPANT DETAILS

Animals and animal care statement

Steap4$^{f/f}$ mice and Steap4-deficient mice in C57BL/6J background were generated as previously described.[14,50] Adiponectin-Cre (028020) and Ucp1-Cre mice (024670) were purchased from The Jackson Laboratory.[51,52] Adipocyte-specific *Steap4*-deficient (*Steap4*^{AKO}) mice were generated by breeding *Steap4* flox/flox (*Steap4*$^{f/f}$) mice to *Adiponectin*-Cre transgenic mice. Thermogenic adipocyte-specific Steap4-deficient (*Steap4*^{BKO}) mice were generated by breeding *Steap4*$^{f/f}$ mice to *Ucp1*-Cre transgenic mice. Sex(male)- and age- matched *Steap4*$^{f/f}$ mice were used as wild-type controls. For all the *in vivo* High Fat Diet model *Steap4*^{AKO} or *Steap4*^{BKO} mice, ~8-week-old mice were maintained on a HFD composed of 60% kcal fat for 12 weeks. Due to the potential impact of hormonal cycles in female mice on dietary studies,[53] all of the mice placed on the HFD were male mice.

Animals were housed in standard SPF facilities with light/dark cycles and were given free access to food and water. All animal procedures were reviewed and approved by the Institutional Animal Care and Use Committee (IACUC) under protocols CWRU 2019-0060/CCF 2020-2316, in compliance with all applicable regulatory policies.

Primary mouse stromal vascular fraction cells (SVFs) and differentiation

In our testing, no sex differences were observed in the outcome of *ex vivo* experiments, therefore stromal vascular fraction cells (SVFs) were harvested from mixed-sex mice at 6-8 weeks of age. The tissues were minced into small pieces, followed by incubation with 3.5 mg/ml Collagenase D in phosphate-buffered saline (PBS) for 60 min in a 37°C shaker water bath. The stromal vascular fraction pellet was collected after 15 min centrifugation at 280 x g and filtered through a 100 μm cell strainer. The cells were cultured in DMEM-F12 medium (10% PBS with 100 IU/ml penicillin and 100 μg/ml streptomycin) until they were confluent, then differentiated in DMEM medium containing 10% PBS with 100 IU/ml penicillin and 100 μg/ml streptomycin, 1 μM dexamethasone, 0.5 mM IBMX, 0.5 μM rosiglitazone and 5 μg/ml insulin for 2 days. Cells were then changed for DMEM complete medium containing 5 μg/ml insulin, every 2–3 days until more than 90% cells were fully differentiated to mature adipocytes. For copper chelator (Bathocuproine disulfonic acid, BCS, Millipore Sigma #146625) and iron chelator (Deferoxamine, DFO, Millipore Sigma #D9533) treatment, 500 μM BCS or 100 μM DFO were added from Day 3 of adipocyte differentiation with DMEM complete medium containing 5 μg/ml insulin until more than 90% cells were fully differentiated to mature adipocytes, and the medium were changed every 2-3 days.

The culture SFVs were authenticated by validating for their ability to differentiate into mature adipocytes and all cells were tested negative for mycoplasma contamination (Invivogen MycoStrip - Mycoplasma Detection Kit).

METHOD DETAILS

Glucose tolerance test (GTT), insulin tolerance test (ITT), and body temperature measurement

For the GTT, mice were fasted overnight, and glucose (2.5 g per kg body weight) was injected peritoneally. For the ITT, mice were fasted for 6 h and insulin (0.75 U per kg body weight) was injected peritoneally. Blood glucose levels were measured using an AimStrip Plus Blood Glucose Testing System (Germaine Laboratories). Rectal temperature was measured using a MicroTherma 2T Handheld Thermometer with a rectal probe (Braintree Scientific).

Indirect calorimetry analysis and EchoMRI

Mice fed a HFD for 12 weeks were allowed to equilibrate to metabolic cage environments for ~48 h before entering into 24h periods at thermoneutrality (30°C), room temperature (22°C) or cold temperature (4°C). Oxygen consumption (VO_2), carbon dioxide production (VCO_2), heat production, and the respiratory exchange ratio were constantly monitored using the Oxymax CLAMS system (Columbus Instruments). The data were normalized to total body weight. Fat mass and lean mass were measured using an EchoMRI-100H system (EchoMRI).

Real-time analysis of OCR

The respiratory activity of adipose tissue was measured using the Seahorse Extracellular Flux XFe24 Analyzer (Agilent).[54] Specifically, iWAT or iBAT was removed, and five pieces (< 5 mg) of tissue were assayed in XFe24 Islet Capture Microplates Four consecutive measurements were obtained in addition to those under basal conditions: (1) after the addition of 20 μg/ml oligomycin; (2) after the sequential addition of 8 μM fluoro-carbonyl cyanide phenylhydrazone; and (3) after the sequential addition of 10 μM rotenone plus 10 μM antimycin A. In this assay, basal oxygen consumption can be established by measurement of the OCR in the absence of drugs.

The maximum OCR occurs after the addition of fluoro-carbonyl cyanide phenylhydrazone since cells attempt to maintain a proton gradient across the inner mitochondrial membrane by increasing the consumption of oxygen by the electron transport chain. All OCR measures were performed three times in a mix–wait–measure cycle of 3-3-3 minutes, respectively.

Co-immunoprecipitation and immunoblot based analysis

Adipose tissue and primary adipocytes were harvested and lysed on ice in a lysis buffer containing 0.5% Triton X-100, 20 mM HEPES (pH 7.4),150 mM NaCl, 12.5 mM glycerophosphate, 1.5 mM MgCl2, 10 mM NaF, 2 mM dithiothreitol, 1 mM sodium orthovanadate, 2 mM EGTA, 20 mM aprotinin and 1 mM phenylmethylsulfonyl fluoride for 20 min, followed by centrifugation at 12,000 x g for 15 min to extract clear lysates (For adipose tissue, tissue was first homogenized and then lysed on ice). Particularly, for Steap4 immunoprecipitation, anti-Steap4 (ProteinTech, 11944-1-AP) antibody was cross-linked to protein A-agarose beads (at least 2 ug antibody per 50 ul protein A-agarose beads) with dimethyl pimelimidate (DMP) (ThermoScientific, 21667) prior to immunoprecipitation using a standard cross-linking method.[55] Lysates were then incubated with antibody-crosslinked protein A- beads at 4°C overnight. After incubation, the beads were washed four times with lysis buffer and the precipitates were eluted with 2 × sample buffer. Elutes and whole-cell extracts were resolved on SDS-PAGE followed by immune blotting with the indicated antibodies. For mitochondrial protein immunoprecipitation, the isolated mitochondrial pellets were lysed in NP40 lysis buffer (1% NP-40, 20 mM Tris-HCl, 150 mM NaCl, protease inhibitor cocktail (Roche), and phosphatase inhibitors (PhosSTOP, Roche), pH 7.4), then the lysates were incubated with antibody-crosslinked A-Sepharose beads at 4°C overnight. After incubation, the beads were washed four times with lysis buffer and the precipitates were eluted with 2 x sample buffer. Elutes and whole-mitochondrial extracts were resolved on SDS-PAGE followed by immune blotting with the indicated antibodies). For other immunoprecipitation assays, the indicated antibodies and Protein A or Protein G beads (without pre-crosslinking) were used following the same procedures.

Immunohistochemistry (IHC) and immunocytochemistry (ICC)

Adipose tissue was fixed in 10% formalin and processed into paraffin blocks at the Cleveland Clinic Imaging Core or AML Laboratories. These paraffin-embedded formalin-fixed iWAT or iBAT depots were sectioned at 5 μm and deparaffinized, followed by epitope retrieval (10 mM Sodium Citrate, 0.05% Tween-20, pH 6.0, 95-100°C ∼ 30 min). Sections on slides were further blocked with 3 % BSA in PBS solution for at least 30 min. Anti-Mac2 monoclonal antibody (Cedarlane, CL8942AP; 0.5 μg/ml) or anti-UCP1 monoclonal antibody (Abcam, ab261912, dilution 1: 50) was incubated at 4°C overnight. Slides were then treated with 0.3% H_2O_2 and incubated with biotinylated secondary antibodies and Peroxidase Streptavidin (Vector Laboratories). For chromogenic detection of horseradish peroxidase (HRP) activity, DAB substrate kit from BD Pharmingen was used. The slides were counterstained with hematoxylin and mounted, then imaged with a light microscope (Keyence BZ-X700 and EVOS M5000 Imaging System). For confocal imaging, SVF cells from iWAT cultured on coverslips were infected with lentivirus encoding mSteap4-GFP (packaged using 293T cells). Four days after infection, the cells were fixed with 4% PFA for 20 minutes. The cells were then blocked with blocking buffer (2% donkey serum, 1% BSA, 0.1% Triton X-100 and 0.025% Tween-20 in PBS, PH7.4) for 30 minutes and stained with Tom20 (Santa Cruz sc-11415, 1:100, diluted in blocking buffer) overnight, followed by donkey anti-rabbit IgG (Alexa Fluo 568) (Thermo Fisher Scientific, A10042, 1:300, diluted in blocking buffer) for 2 hours. The stained cells were then mounted with ProLong Gold Antifade Reagent with DAPI (Thermo Fisher Scientific, P36931) followed by image analysis. Cells were washed with PBS between steps.

Mitochondrial isolation and blue native polyacrylamide gel electrophoresis (BN-PAGE)

Mitochondrial isolation was performed according to an established protocol.[56] ∼150 mg of iWAT or iBAT specimen were homogenized in 2 ml ice-cold isolation buffer using a Teflon Potter Elvehjem homogenizer. After homogenization, the specimen was centrifuged at 500 g for 10 min, and the mitochondrial fractions were further washed and pelleted at 7,000 g for 10 min for three times. The mitochondrial pellets were lysed in mitochondrial lysis buffer (50 mM Bis-Tris (pH 6), 50 mM NaCl, 10% wt/vol glycerol and 2% digitonin and protease inhibitors) following two rounds of centrifugation at 20,000 g for 30 min, and the clear supernatants were collected for BN-PAGE. Proteins were quantified using BCA assay (Thermo Fisher Scientific). Then 20 mg of mitochondrial lysates with G-250 Coomassie were loaded into 3 –12% NativePAGE Novex Bis-Tris Gels (Invitrogen, BN1001BOX) in an Xcell SureLock tank (Invitrogen), run and transferred onto a polyvinylidene difluoride (PVDF) membrane at 4°C. After transfer, the membrane was rinsed with 8% acetic acid for 15 min and air-dried. Membranes were blocked with 5% blotting-grade blocker (Bio-rad, 1706404) prepared in Tris buffered saline + 0.1% Tween 20 (TBST) and incubated overnight at 4°C with antibodies: anti-NDUFA9, anti-SDHA, anti-Ubiquinol-Cytochrome C Reductase Core Protein I, anti-MTCO1, and total OxPhos Rodent WB Antibody Cocktail. Coomassie blue images were from parallel gels with same samples.

Nuclei isolation

Nuclei isolation kit (NUC-101, Millipore Sigma) was used to isolate nuclei from differentiated SVFs. Tissue culture dishes containing Steap4 WT and KO SVF cells (2 150 mm diameter dishes each genotype) differentiated on day 6 were washed with 10 ml ice-cold PBS. For each genotype (WT and KO), 4 ml of ice-cold Nuclei EZ lysis buffer was added, and cells were harvested and lysed. The total cell lysate from each genotype was transferred to a separate 15 ml tube, vortexed and placed on ice for 5 min. Nuclei were then collected by centrifugation at 500 x g for five minutes at 4°C. The supernatant containing cytoplasmic components was saved for

later western-blot analysis. For each sample, nuclei were then resuspended and washed in 4 ml ice-cold Nuclei EZ Lysis Buffer for 5 minutes on ice. The washed nuclei were then collected by centrifugation at 500 x g for five minutes at 4°C. Each pellet was further resuspended in 200 μl of ice-cold Nuclei EZ Storage Buffer. Sonication was performed to prepare lysates (in the presence of protease inhibitor cocktail and phosphatase inhibitors (PhosSTOP, Roche) for western-blot analysis.

Real-time qPCR

Total RNA was extracted using RNeasy Lipid Tissue Mini Kit (Qiagen) according to the manufacturer's instructions. 2 μg total RNA for each sample was reverse-transcribed using SuperScript II Reverse Transcriptase. The resulting complementary DNA was analyzed by real-time qPCR with indicated primers using SYBR Green Real-Time PCR Master Mix (Applied Biosystems).

Transmission electron microscopy

For ultrastructural analysis, freshly dissected iBAT from HFD-fed *Steap4*$^{f/f}$ and *Steap4*^{AKO} mice were cut into 2 mm × 1 mm × 1mm and were fixed for 1 h at 22°C in 2% paraformaldehyde, 2.5% glutaraldehyde (Polysciences), and 0.05% malachite green (Sigma-Aldrich) in 100 mM sodium cacodylate buffer (pH 7.2). Malachite green was incorporated into the fixative for stabilization of lipid constituents soluble in aqueous glutaraldehyde. Samples were washed in cacodylate buffer and were post-fixed for 1 h in 1% osmium tetroxide (Polysciences). Samples were then rinsed extensively in distilled water before *en bloc* staining for 1 h with 1% aqueous uranyl acetate (Ted Pella). Following several rinses in distilled water, the samples were dehydrated in a graded series of ethanol and embedded in Eponate 12 resin (Ted Pella). Sections 95 nm in thickness were cut with a Leica Ultracut UC7 ultramicrotome (Leica Microsystems), then stained with uranyl acetate and lead citrate and viewed on a Tecnai G2 Spirit BioTWIN transmission electron microscope (FEI) at 60 kV.

Proteomic analysis of Steap4-interacting proteins

WT and Steap4 KO SVFs (preadipocytes) and *ex vivo* differentiated primary adipocytes were immunoprecipitated using an anti-Steap4 antibody for proteomic analysis (described in co-immunoprecipitation above). Samples were submitted for in-gel digestion in the Proteomics Core at Lerner Research Institute. For the protein digestion, the bands were cut to minimize excess polyacrylamide, divided into a number of smaller pieces. The gel pieces were washed with water and dehydrated in acetonitrile. The bands were then reduced with DTT and alkylated with iodoacetamide prior to the in-gel digestion. All bands were digested in-gel using trypsin, by adding 5 μL of 10 ng/μL trypsin in 50 mM ammonium bicarbonate and incubating overnight at room temperature to achieve complete digestion. The peptides that were formed were extracted from the polyacrylamide in two aliquots of 30 μL 50% acetonitrile with 5% formic acid. These extracts were combined and evaporated to <10 μL in Speedvac and then resuspended in 0.1% formic acid to make up a final volume of ~30 μL for LC-MS analysis. The LC-MS system was a Bruker TimsTof Pro2 Q-Tof mass spectrometry system. The HPLC column was a Bruker 15 cm x 75 μm id C18 ReproSil AQ, 1.9 μm, 120 Å reversed-phase capillary chromatography column. One μL volumes of the extract were injected and the peptides eluted from the column by an acetonitrile/0.1% formic acid gradient at a flow rate of 0.3 μL/min and directly introduced into the source of the mass spectrometer. The digests were analyzed using positive ion mode, coupled with a CaptiveSpray ion source (both from Bruker Daltonik GmbH, operating Bremen) Parallel Accumulation–Serial Fragmentation DDA was used to select precursor ions for fragmentation with a TIMS-MS scan followed by 10 PASEF MS/MS scans. The TIMS-MS survey scan was acquired between 0.60 and 1.6 Vs/cm^2 and 100–1,700 m/z with a ramp time of 166 ms. The total cycle time for the PASEF scans was 1.2 seconds and the MS/MS experiments were performed with collision energies between 20 eV (0.6 Vs/cm^2) to 59 eV (1.6 Vs/cm^2). Precursors with 2–5 charges were selected with the target value set to 20,000 a.u and intensity threshold to 2,500 a.u. Precursors were dynamically excluded for 0.4 s. The data were analyzed by using all CID spectra collected in the experiment to search the mouse SwissProtKB database containing 17,552 entries using the program MSFragger 3.4. Proteins of moderate to high abundance (spectral counts ≥ 10) that are more enriched in WT mature adipocytes versus WT preadipocytes or *Steap4* KO cells (≥ 2-fold increase in spectral counts) were reported as Steap4-interacting proteins.

Subcellular localization analysis

Among the 91 proteins that interact with Steap4, the localization analysis was conducted on the subset of 89 proteins for which localization information is available in the COMPARTMENTS database. Specifically, COMPARTMENTS assess each protein its localization in 11 compartments, including nucleus, cytosol, cytoskeleton, peroxisome, lysosome, endoplasmic reticulum, Golgi apparatus, plasma membrane, endosome, extracellular space, and mitochondrion. The confidence of these protein-compartment associations was accessed by a score integrating manually curated literature, high-throughput screens, automatic text mining, and sequence-based prediction methods. This score ranges from zero (i.e., no evidence) to five. Further localization analysis utilized the Mouse MitoCarta3.0 dataset (2020 release), which includes 1140 mitochondrial mouse genes. After identifying human homologues of the Steap4 interacting proteins using the Ensembl Biomart database (version 2.52.0), the localization of these human proteins was further assessed using The Human Protein Atlas (version 21.1).[57] The localization analysis focused on the subset of 76 proteins for which localization information is available in The Human Protein Atlas database. Additionally, similar analysis was conducted using the MitoCoP dataset, which contains over 1100 high-confidence human mitochondrial proteins.

RNA-seq analysis

Total RNA was extracted from iWAT of HFD-fed *Steap4*$^{f/f}$ and *Steap4*^{AKO} mice with the Qiagen RNeasy Lipid Tissue Mini Kit following the manufacturer's instructions. Sequencing library preparation and RNA-seq were conducted by Novogene. mRNA was purified from total RNA using poly-T oligo-attached magnetic beads. The library preparations were sequenced on an Illumina platform and paired-end reads were generated. Raw data (raw reads) of fastq format were processed to obtain clean data (clean reads) by removing reads containing adapter, reads containing ploy-N and low-quality reads from raw data. We then aligned RNA-Seq reads to the mouse reference genome (GRCm38/mm10) using STAR (version 2.7.0e) with the transcript annotation supplied. Both the mouse reference genome and transcript annotation were downloaded from UCSC Genome Browser. We then assigned the mapped reads to gene using RSEM (version 1.3.3), with default union-counting mode. To perform differential gene expression analysis, we applied DESeq2 R package (R 4.2.0, DEseq2 version 1.12.4), with an adjusted P-value of 0.05 as the cutoff.

For STEAP4 expression crossing various human tissues including adipose tissue, the data used for the analyses described in this paper were obtained from the GTEx Portal (Release V10.).

Gene Ontology enrichment analysis and visualization

Gene Ontology (GO) enrichment analysis was performed on the Web server of the Database for Annotation, Visualization, and Integrated Discovery (DAVID) functional annotation tool (https://david.ncifcrf.gov/tools.jsp). A false discovery rate of 10% was applied to evaluate significance. We then adapted GOPlot R package (version 1.0.2) to visualize the gene set annotation enrichment analysis results.

Differential splicing analysis

RNA-Seq reads were aligned to the UCSC mouse reference genome (GRCm38/mm10) using STAR (version 2.7.0e). The aligned BAM files were indexed by 'samtools' (version 1.8) and then proceeded to create junction files by 'regtools' (version 0.6.0) for downstream analysis. We performed differential splicing analysis using intron-centric package 'LeafCutter' (version 0.2.9). The introns in each file were clustered using 'leafcutter_cluster_regtools.py.script'(python version 3.8.6), requiring 50 split reads supporting each cluster and showing intron of up to 500kb (input flag -m 50 -o -l 500000). Differential splicing was then evaluated using the 'leafcutter_ds.R' (R version 4.2.0) script with using the exons file provided by using the 'gtf_to_exons.R' script to convert GTF file to the required format. LeafCutter reported the splice clusters that have significantly different usage between Steap4 KO and WT (FDR<10%). The interactive visual web serve was then created using 'ds_plots.R' script.

Validation of differential splice events from LeafCutter

To validate differential splicing events identified by the LeafCutter program, we used an RT-PCR approach. Total RNA was extracted using RNeasy Lipid Tissue Mini Kit (Qiagen, Cat#74804) following the manufacturer's instructions. 2 μg of DNase-treated RNA was reverse-transcribed (Thermo Fisher Scientific) according to the manufacturer's instructions. KOD Hot Start DNA Polymerase (Millipore Sigma) was used for RT-PCR with sequence-specific primers. Conditions for PCR are as follows: initial denaturation at 95°C for 2 min, 35 cycles of (95°C, 20 sec; annealing at 55° or 60°C, 10 sec; extension at 70°C, 5 sec). RT-PCR products were subjected to agarose gel electrophoresis and imaged using GE AI680 Imager or Syngene Imager and quantified by Image Lab 6.1 Software (Bio-Rad Laboratories Inc.).

Spectrophotometric assays of mitochondrial respiratory complex activity

The activities of mitochondrial respiratory complexes were assayed spectrophotometrically using sonicated, thawed mitochondria samples at 22°C[58,59]. For the complex I (NADH-ubiquinone reductase) activity assay, the electron transfer activity of complex I was assayed by ubiquinone-stimulated NADH oxidation. For this, 5 mg of mitochondrial protein was mixed with 100 μl assay buffer (20 mM potassium phosphate buffer, 2 mM NaN_3, 0.8% sodium cholate and 0.15 mM NADH (pH 8.0)). The reaction was initiated by the addition of 0.1 mM ubiquinone-1 (CoQ1) and the change of absorbance for NADH was measured at 340 nm ($\varepsilon = 6.22\ mM^{-1}\ cm^{-1}$). The specificity of the assay was validated by rotenone-sensitive inhibition. Complex I activity was expressed as the oxidation rate of NADH (nmol NADH oxidized per min per mg protein). For the complex III (ubiquinol-cytochrome *c* reductase) activity assay, complex III activity was evaluated by ubiquinol-mediated ferricytochrome *c* reduction at 550 nm ($\varepsilon = 18.5\ mM^{-1}\ cm^{-1}$) upon the addition of 1 μg protein to 100 μl assay buffer (50 mM potassium phosphate buffer, 1 mM EDTA, 50 μM cytochrome *c*, 0.1% sodium cholate, 2 mM NaN_3 and 25 μM ubiquinol (pH 7.0)). Inhibition of the assay with antimycin A was used to verify the specificity of the assay. Complex III activity was expressed as the reduction rate of ferricytochrome *c* (nmol ferricytochrome *c* reduced per min per mg protein). For the complex IV activity assay, 5 mg of mitochondrial protein were added to 600 μl assay buffer. The assay buffer contained 50 mM phosphate buffer and 60 μM ferrocytochrome *c* (pH 7.4). Complex IV activity was determined by the decrease in the rate of absorbance of ferrocytochrome *c* at 550 nm ($\epsilon = 18.5\ mM^{-1}\ cm^{-1}$). Potassium cyanide was used as the inhibitor to validate the assay. Complex IV activity was expressed as the oxidation rate of ferrocytochrome *c* (nmol ferrocytochrome *c* oxidized/min/mg protein).

QUANTIFICATION AND STATISTICAL ANALYSIS

The nature of tests, n and meaning of bars, lines and error bars are indicated in the figure legends. Generally, significance of differences between two groups was determined by unpaired (Student's) t-test(two-tailed). Differences were considered significant at

$p < 0.05$. Statistical significance is given as * $0.01 \leq p < 0.05$, ** $0.001 \leq p < 0.01$, *** $p < 0.001$.; or ns, not significant ($p \geq 0.05$). All data represent means ± s.e.m. Detailed P-value information calculated by and exported from GraphPad Prism is provided in the Table S9. For all cases where $p < 0.0001$ (belonging to the "***" catalog in the manuscript), Prism displays only "****" and " $p < 0.0001$", where the p value was then provided based on the Excel formula "T.DIST.2T(T, df)" , in the Table S9, as suggested by GraphPad "KNOWLEDGEBASE - ARTICLE #687". All image/data analyses were performed using ImageJ Software (National Institutes of Health), Image Lab 6.1 (Bio-rad) or GraphPad Prism 9 software (Dotmatics). Additionally, Fisher's exact test was applied to assess the association between two variables. The test was conducted using the fisher.test() function with default settings (two-tailed) from the stats package (version 4.2.1) in R. Statistical significance was defined as $p < 0.05$.